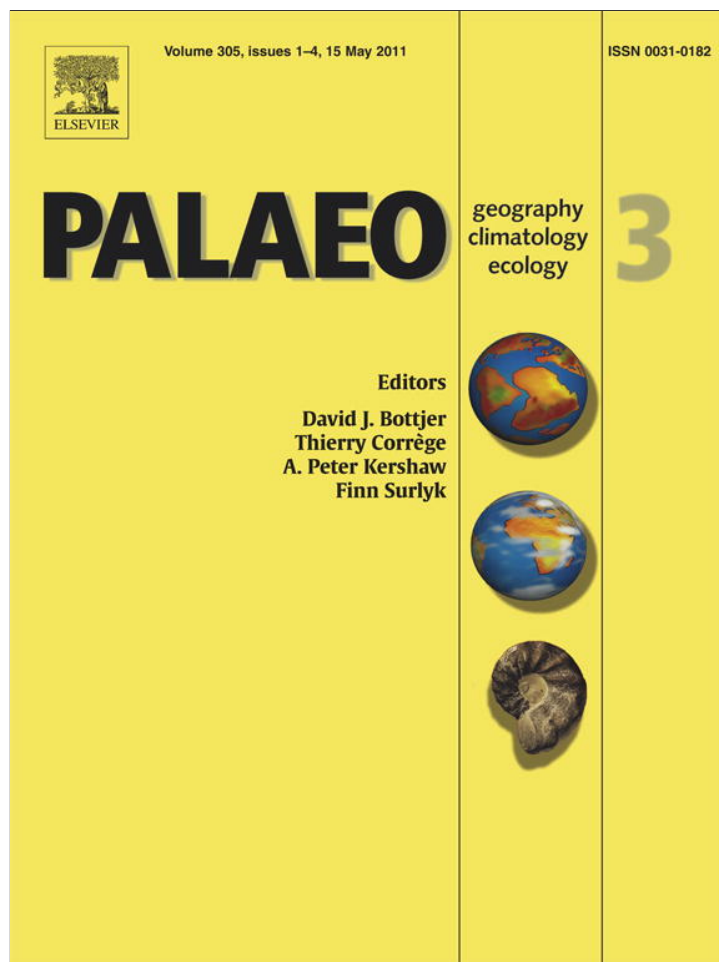


Provided for non-commercial research and education use.
Not for reproduction, distribution or commercial use.



This article appeared in a journal published by Elsevier. The attached copy is furnished to the author for internal non-commercial research and education use, including for instruction at the authors institution and sharing with colleagues.

Other uses, including reproduction and distribution, or selling or licensing copies, or posting to personal, institutional or third party websites are prohibited.

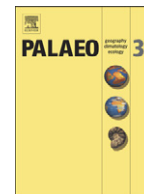
In most cases authors are permitted to post their version of the article (e.g. in Word or Tex form) to their personal website or institutional repository. Authors requiring further information regarding Elsevier's archiving and manuscript policies are encouraged to visit:

<http://www.elsevier.com/copyright>



Contents lists available at ScienceDirect

Palaeogeography, Palaeoclimatology, Palaeoecology

journal homepage: www.elsevier.com/locate/palaeo

A 250 ka sedimentary record from a small karstic lake in the Northern Levant (Yammoûneh, Lebanon) Paleoclimatic implications

A.-L. Develle ^{a,*}, F. Gasse ^a, L. Vidal ^a, D. Williamson ^b, F. Demory ^a, E. Van Campo ^c, B. Ghaleb ^d, N. Thouveny ^a^a CEREGE, UMR 6635, Europôle de l'Arbois, BP80, 13545 Aix en Provence Cedex 4, France^b Laboratoire d'Océanographie et du Climat: Expérimentations et Approches Numériques, UMR 7159 CNRS/IRD, France^c ECOLAB, UMR 5245 (CNRS-Université de Toulouse-INPT), BP 24349, 31062 Toulouse Cedex 9, France^d GEOTOP, université du Québec à Montréal, Case postale 8888, succursale A, Montréal, Québec, Canada H3C 3P8

ARTICLE INFO

Article history:

Received 21 September 2010

Received in revised form 9 February 2011

Accepted 10 February 2011

Available online 17 February 2011

Keywords:

Lake

Carbonates

Sedimentology

Paleomagnetism

Eastern Mediterranean

Glacial–interglacial variability

ABSTRACT

The Levant, influenced by both the Mediterranean Sea and the Saharan–Arabian deserts, is a key region for understanding climatic changes in response to glacial/interglacial boundary conditions that have greatly affected regional hydrology. Here, we present the first long-term paleoenvironmental record from the northern Levant, presently much wetter than the southern Levant. Our record derives from the multi-proxy study of a sediment core (36 m long) retrieved from the small intra-mountainous, tectonic basin of Yammoûneh (Lebanon), which is mainly supplied by karstic springs.

Sediments consist of a thick accumulation of brownish to greenish clayey silts, interrupted by intervals of whitish marls composed of CaCO₃ rich material. The core chronology is based on radiometric dating (¹⁴C and U/Th) and paleomagnetic techniques. The sedimentary sequence spans approximately the last two glacial–interglacial cycles (~250 ka). Carbonate content is relatively high throughout the profile due to a perennial input of detrital calcite from the watershed, but varies significantly. The marls are mostly composed of authigenic and biogenic calcite and reflect lacustrine environments with high carbonate productivity during peaks of interglacial periods. Their occurrence suggests low physical erosion of the basin slopes which were covered by arboreal vegetation, and intense karstic water circulation under warm and relatively wet conditions, in agreement with pollen data. The clayey silts are dominated by quartz and clay minerals, and a few amounts of K-feldspars and dolomite. They are characterized by high concentration in magnetic particles, and high relative concentrations of Si, Al, K and Fe considered as strictly of detrital origin. Due to the carbonated nature of the watershed, quartz and K-feldspars are attributed to eolian origin from a distal source. The clayey silt intervals generally suggest palustrine conditions with abrupt flows responsible for runoff-derived material, or subaerial environments and low local water availability in particular during the Last Glacial Maximum. High Si/Al and K/Al ratios, during interglacials, are attributed to relatively high eolian dust contribution due to the decrease of local detrital inputs.

Our study reveals significant differences between Yammoûneh and lake records from the Dead-Sea basin (southern Levant), the latter showing high/low levels during glacial/interglacial periods. These hydrological differences might reflect either changes in the North–South (NS) rainfall gradient in response to the development of the northern ice sheet and the southward migration of the westerly belt, or local factors, i.e., a decrease in efficient precipitation and water availability at Yammoûneh during the coldest glacial periods (e.g., the Last Glacial Maximum), due to water storage by ice caps on the Mount Lebanon range and frozen soils in the Yammoûneh basin.

© 2011 Elsevier B.V. All rights reserved.

1. Introduction

The Levant (Fig. 1) exhibits a large variety of landscapes resulting from (i) its climatic setting at the transition between the temperate Mediterranean domain and the subtropical desert belt, and (ii) its steep topographic gradients. The region experiences a Mediterranean

climate, with cool-wet winters and hot-dry summers. Winter rainfall comes from Atlantic–Mediterranean fronts steered eastward by the mid-latitude westerlies (Ziv et al., 2010) (Fig. 1a), but precipitation diminishes with latitude from north to south, and from west to east due to the orographic effect of the mountain ranges running parallel to the Eastern Mediterranean Sea coast and distance from the sea coast (Fig. 1b). Water resources are vulnerable and climate changes seriously impact human societies. The Levant has experienced a long history of cultural dynamics since the Paleolithic (Henry, 2003),

* Corresponding author. Tel.: +33 381 666 431.

E-mail address: anne_lise.develle@univ-fcomte.fr (A.-L. Develle).

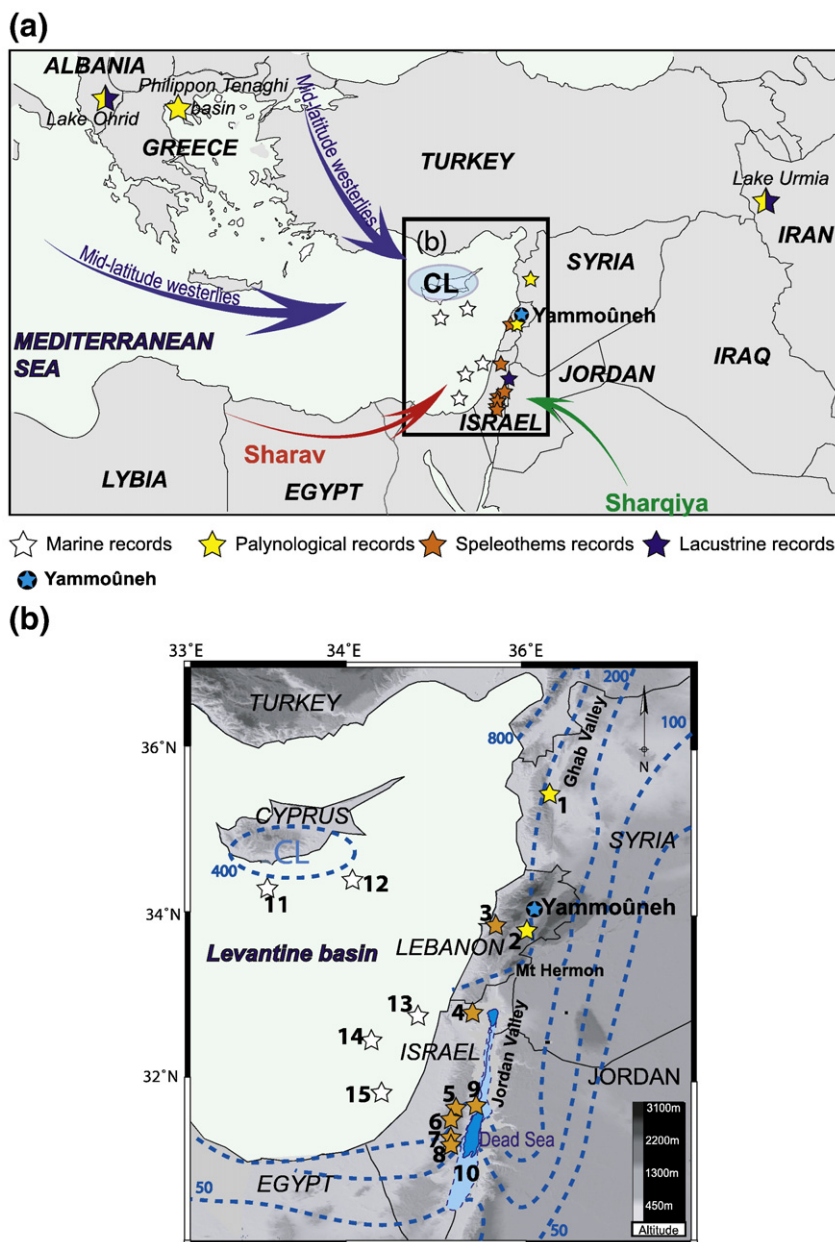


Fig. 1. (a) Eastern Mediterranean map showing the localisation of the Northern Mediterranean sites cited in the text: Lake Ohrid (Albania, Lézine et al., 2010); Tenaghi Philippon basin (Greece; Tzedakis, 1993) and Lake Urmia (Iran; Djamali et al., 2008). Scheme of the major wind trajectories over Eastern Mediterranean. (<http://iridl.ldeo.columbia.edu/maproom>; Alpert and Ziv, 1989; Saaroni et al., 1998): In blue: mid-latitude westerlies responsible for the winter precipitation. In Red: occasional wind storms coming from the Sharav cyclone. In green: occasional wind called Sharqiya. (b) The Levant. Isohyets showing the NS and EW precipitation gradients (CL: Cyprus Low). Location of Yammoûneh and Levantine sites of Late Pleistocene-Holocene paleoclimatic records cited in the text, and numbered 1 to 15: (1) Ghab valley (Wu et al., 2007), (2) Ammiq-Bekaa valley (Hajar et al., 2008), (3) Jeita cave (Nader et al., 2007; Verheyden et al., 2008); (4) Peqiin cave (Bar-Matthews et al., 2003); (5) Jerusalem west cave (Frumkin et al., 1999, 2000; Frumkin and Stein, 2004); (6) Soreq cave (Bar-Matthews et al., 1997, 2003); (7) Ma'ale Dragnot, (8) Tsavoia and (9) Ma'ale Efrayim caves (Vaks et al., 2003, 2006, 2007, 2008); (10) Lakes of the Dead Sea basin (Waldmann et al., 2010); (11) ODP 967 (Emeis et al., 2003); (12) MD9501; (13) SL 112 (Hamann et al., 2008), (14) MD94-632 (Essallami et al., 2007) and (15) MD9509. Records derived from marine studies (in white), lake level reconstructions (in blue), speleothems (orange stars), pollen (yellow stars). Note that the area of paleolake Lisan (Dead Sea basin) shown here is that of its maximum extent (26–24 ka; Bartov et al., 2003).

which has often been associated with climatic changes (Bar-Yosef, 2003; Migowski et al., 2006; Staubwasser and Weiss, 2006; Vaks et al., 2007; Waldmann et al., 2010). Reconstructing past environmental conditions is essential for understanding the response of Eastern Mediterranean (EM) regions to global climatic changes and the varying environmental contexts where ancient human groups evolved. However, the variability of the terrestrial water cycle is not fully established in this region of sharp climatic gradients. In the southern Levant (Israel mainly), paleolake and speleothem studies have already provided well-dated, high resolution records spanning

several glacial/interglacial cycles, while no long-term paleoclimatic reconstruction is available from the northern Levant (Syria, Lebanon). Furthermore, interpretations of the records are sometimes difficult to reconcile. Lakes and paleolakes from the Dead Sea-Jordan Valley basin experienced generally high stands attributed to increased precipitation during glacial periods, and arid conditions during interglacials (Enzel et al., 2008; Waldmann et al., 2010). In the rain shadow of the Judean Mountains, speleothem growth tended to stop during interglacials indicating a P-E deficit (Vaks et al., 2003, 2006), as in the Dead Sea lakes. Nevertheless, interglacial periods were

punctuated by wet pulses, also recorded by travertines and speleothems in the Negev Desert, and attributed enhanced Atlantic-Mediterranean cyclones (Vaks, 2007; Vaks et al., 2008), or to intrusions of moisture from southern sources (Waldmann et al., 2010). In northern and central Israel, isotope records of speleothems located west and north west of the Dead Sea Basin have been interpreted as indicator of rainfall amount, suggesting wet/dry interglacial/glacial periods, e.g., at Soreq and Peqiin Caves (Bar-Matthews et al., 1997, 2003), or as reflecting the isotopic composition of the moisture source (the EM basin) based on Jerusalem West Cave and Lake Lisan aragonite isotope records according to Frumkin et al. (1999) and Kolodny et al. (2005), respectively. The later interpretations are in better agreement with the lake level fluctuations in the Dead Sea Basin (DSB). Clearly more information is needed to assess a more robust picture of the hydrological variability in this region.

Here, attention is paid to late Quaternary terrestrial environmental and climatic changes in Lebanon on the glacial/interglacial time-scale. The present paper provides a new paleoenvironmental record from Lebanon spanning approximately the past 250 ka. This record partly fills the North–South disparity in spatial data coverage in the Levant region, and may help understand the spatial heterogeneity, if any, of the paleoclimatic patterns. Our record comes from a 36 m-long sediment core retrieved from a small, intra-mountainous lake basin (Yammoûneh). Although located at only 100 km from Mt Hermon (the head water area of the Jordan-Dead Sea basin), this lake strongly differs from those in the Dead Sea Basin by its very small size, its higher elevation and its rapid throughflow. We focus on sedimentological indicators with four main aims: (1) identify the major sedimentary changes from a multi-proxy approach including X-Ray Diffractometry, elemental X-Ray Fluorescence analyses and sediment magnetic properties; (2) establish the chronology of past environmental fluctuations (^{14}C , U/Th dating, magnetostratigraphy); (3) examine the potential processes responsible for sedimentary changes and (4) discuss the impacts of site-specific factors versus those of regional and global climate changes through comparison with other long-term records from the region.

2. Modern setting

The Yammoûneh basin (34.06°N–34.09°N, 36.0°E–36.03°E), 1360 meters above sea level (m a.s.l.), 6 km long, 2 km wide, is located on the eastern flank of Mount Lebanon, approximately 37 km from the Mediterranean Sea shore. Since at least Roman times (Besançon, 1968), a shallow seasonal lake occupied the southern part of the basin (Fig. 2b). The lake was drained in the early 1930s following the construction of an underground duct designed to transport water for irrigation of the Bakka plain located eastward (Fig. 2a). Before this man-made drainage, the lake developed in March–April for a mean duration of 5 months and may have reached a depth of 2 m (dry years) to 10 m (wet years) (Besançon, 1968). The rather flat basin floor is today entirely cultivated.

2.1. Geology and geomorphology

The major structures of the Levant are related to the Levant Fault System (LFS; Le Pichon and Gaulier, 1988), which connects the NW tip of the Red Sea to the SW end of the East Anatolian Fault. South and north of Lebanon, the Levant Fault System activity have generated the large tectonic basins of the Dead Sea (Dead Sea–Jordan Valley–Lake Tiberias) and the Ghab Valley (Fig. 1b). The Lebanon structure is more complex since the Lebanese section of the Levant Fault is divided into several branches and veers to the right, forming a restraining bend responsible for the high reliefs of Mount Lebanon (Daëron et al., 2007). The main geomorphic features of Lebanon run roughly parallel to the Mediterranean coastline (SSW–NNE) and consist of a narrow

coastal plain, the Mount Lebanon range with its peak at 3083 m a.s.l., the Bakka plain (ca. 900 m a.s.l.) and the Anti-Lebanon mountains (2000 m a.s.l.).

The Yammoûneh basin is a small tectonic (pull-apart) depression along the Yammoûneh Fault, one of the major branches of the LFS (Fig. 2b). Its long axis strikes SSW–NNE. The basin is inset between thick subtabular sequences of intensively karstified Cenomanian dolomitic limestones (Dubertret, 1975; Hakim, 1985). West of Yammoûneh, the karstic Jabal Mnaitra plateau abruptly rises to 2100 m a.s.l. (Fig. 2a). To the East, the Yammoûneh plain is separated from the Bakka (Fig. 2a) by gently sloping hills (Jabal el-Qalaa, 1500 m a.s.l.; Fig. 2b). In its southern part, patches of whitish lacustrine deposits indicate the ancient lake area, while reddish coarse material in the north represents the alluvial deposits of the small Ainata river flowing from the eastern flank of Mt Lebanon. Using the Rivertools (Peckham, 2003) and SWAT2005 (Arnold et al., 1998) softwares, the area of the basin's surface watershed was estimated from digital elevation models at 103–109 km² (Fig. 2b). Lithological formations outcropping in the watershed are Cenomanian limestones and red fersiallitic soils described as typical across Lebanon (Lamouroux, 1972). The alluvial fans that border the western border of the basin are composed of a mixture of these red soils, detrital carbonates particles derived from the bedrock and calcareous concretions.

2.2. Climate

Winter rainfall in the Levant is controlled by the Mediterranean Sea and the dynamics of the mid-latitude cyclones that developed over the Sea during winter (Sharon and Kutiel, 1986; Gat et al., 2003; Ziv et al., 2010). Cold air masses arrive from the Atlantic and northern Europe and tend to propagate eastward. These air masses travel over the relatively warm Mediterranean and become saturated by moisture. The dynamics of the Mediterranean cyclones imply the intersection of the northwesterly–westerly flows (Fig. 1a) with the EM shoreline and, later on, with the mountain ridges and result in intensive rainfall over the Levant (Ziv et al., 2006). Rainfall spatial and temporal variability is related to the activity and position of the Cyprus Lows generally located south of Turkey (Fig. 1). In summer, when the westerly belt is shifted to the north and the EM sea level pressure is reinforced, the region experiences hot and dry conditions. On the southernmost Levant, only, exceptional rainfall events occur in fall and spring in the southern Levant and are most commonly linked to a stronger Red Sea Low (Kahana et al., 2002; Ziv et al., 2005).

Precipitation and temperature vary considerably in relation to topography and distance from the sea. In Lebanon, mean annual precipitation (MAP) ranges between 700 and 1000 mm along the coast to >1400 mm in Mount Lebanon; it decreases to 400 mm in the Bakka plain. Above 2000 m a.s.l., precipitation is essentially niveous (Service Météorologique du Liban, 1973; Abi-Saleh and Safi, 1988; Karam, 2002). At Yammoûneh, the rainfall regime resembles that of the western flank of Mount Lebanon (MAP: 900–1000 mm/year, as snow falls over about 30 days/year), but continentality is marked by large diurnal and seasonal variations in temperature and air humidity. While mean annual temperature is about 15 °C, means of temperature minima of the coldest month and of temperature maxima during the warmest month are –4.2 °C and 34.6 °C, respectively. Freezing occurs over 3 months/year. Relative air humidity varies between about 70% in winter and 45% in summer. The wet-cold season takes place from November to March and the dry-warm season lasts 5 months (May–October).

Most wind storms over the Levant occur in winter and follow the dominant direction of the westerlies (Fig. 1a). Occasionally, more local winds influence the region. The *Sharav* cyclone, typical of the spring season, originates over Libya and Egypt and moves eastward along the North African coast (Winstanley, 1972; Alpert and Ziv, 1989). When approaching Sinai, it sometimes turns to the north, following the

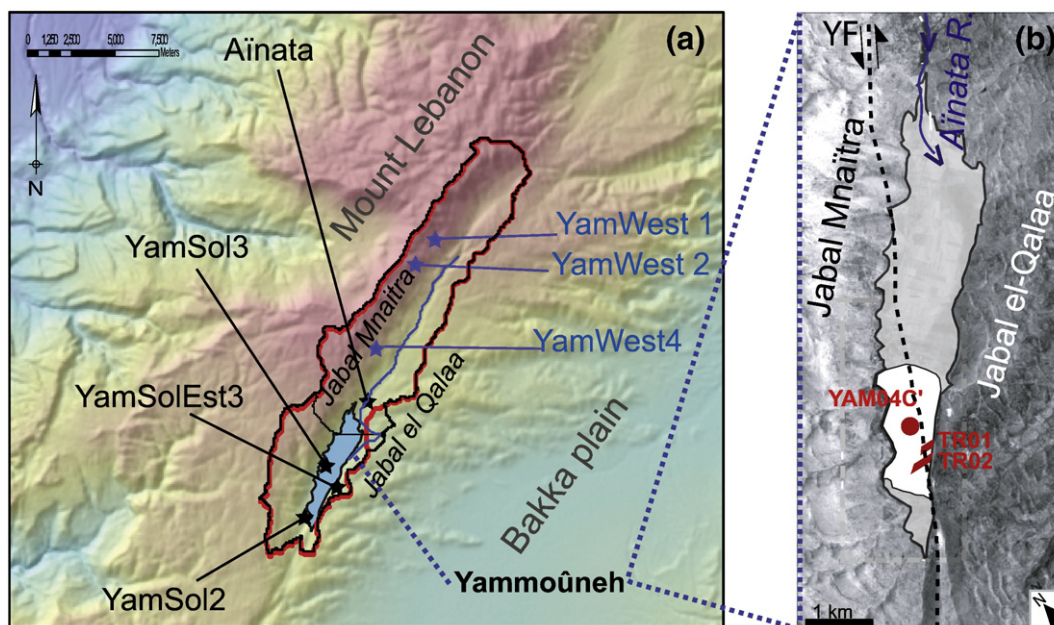


Fig. 2. (a) Main structure and surface watershed of the Yammoûneh basin estimated from a Digital Elevation Model using Rivertools (red) and SWAT2005 (black) softwares. Stars indicate the positions of the soils (black stars) and bedrocks (blue stars) analyzed in this study. (b) The Yammoûneh depression and approximate paleolake area (in white) with location of the sedimentary profiles TR01 and TR02 (trenches) and YAM04C' (piston core). The black dashed line is the surface trace of the Yammoûneh Fault; black arrows show the direction of lateral movement along the fault (modified from Daëron, 2005). YF: Yammoûneh fault.

direction of the EM coastline (Fig. 1a). Winds resulting from this cyclonic activity, commonly called *Sirocco* or *Khamsin*, sometime cause warm and dry conditions associated to heavy sand and dust storms in the region (Alpert and Ziv, 1989; Stanley and Wingerath, 1996; Saaroni et al., 1998; Goudie and Middleton, 2001). Saaroni et al. (1998) also described strong easterly winds, called *Sharqiya*, which develop during winter and early springs over the Near East and bring dust storms from Arabia to the Levantine area (Fig. 1a), and sometimes converge with the *Sharav* winds. Winds crossing Lebanon are consistent with these general circulation trends, although during winter cold northerly winds may exert a greater influence than southward winds.

2.3. Hydrological setting of the Yammoûneh basin

Besides direct precipitation ($<1.2 \cdot 10^6 \text{ m}^3/\text{year}$), the Yammoûneh basin largely depends on precipitation over the western highlands. The Jabal Mnaïtra plateau is incised by gullies that terminate with alluvial fans nearly to the basin floor. The surface network captures rainfall and snowmelt water from the Jabal Mnaïtra heights and redirects it into the basin through runoff. Water inputs from the eastern slopes are relatively small as most of the wadis formed from the Jabal el-Qalaa are drained toward the Bakka plain. The most important water inflow to Yammoûneh comes from perennial karstic springs ($35\text{--}70 \cdot 10^6 \text{ m}^3/\text{year}$; Besançon, 1968; Hakim, 1985). Beneath the Jabal Mnaïtra plateau, subterranean karstic networks collect snowmelt-water feeding a dozen springs along the western edge of the basin. Studies of nearby aquifers show that water residence time in such systems (1 season to 2–3 years; Aouad et al., 2004; El-Hakim, 2005). The spring discharge, reaching its maximum over late spring and early summer, delivers relatively cold (average temperature: 7°C), calcium-rich, circumneutral freshwater all year round (Hakim, 1985). Following the smooth slope of the basin, sinuous channels drain the spring and runoff water into karstic sinkholes along the opposite eastern border. The karstified, intensively fissured and faulted basin floor is highly permeable. Leakage through the lake bottom has always reduced the lake water residence time, water

depth and salt content. Despite the absence of surface outlet, the basin is hydrologically open with rapid throughflow.

3. Material and methods

3.1. Material

This paper concerns the upper 36 m of one of the sediment cores (YAM04C', 73 m; sediment recovery: $\sim 80\%$) collected in 2004 from the central part of the Yammoûneh paleolake (Fig. 2b). The coring was performed using a SEDIDRILL drilling machine equipped with Mazier and cable corers. This coring came after detailed geoelectric investigations (A. Sursock and R. Jomma, pers. comm., 2004) and neotectonic studies of the Yammoûneh Fault (Daëron et al., 2004, 2007; Daëron, 2005), for which two trenches (Fig. 2b) were dug throughout the fault in 2001 (TR01, 5 m-deep, 75 m-long) and 2002 (TR02, 9 m-deep, 50 m-long) and were ^{14}C -dated (Daëron et al., 2007, and pers. comm). These trenches were stratigraphically correlated with the upper part of the core (Develle et al., 2010) and are only considered here for stratigraphical control.

A simplified stratigraphic log of the upper 36 m of YAM04C' is presented in Fig. 3. A more detailed description is given in Appendix A. Based on macro- and microscopic (smear slides) observations, the profile can be schematically divided in 10 major lithological units, noted I to X (Fig. 3).

Four units (Units I, IV, VI and IX), each a few meters thick, consist of light lacustrine carbonate having a powdery or sandy texture and rich in remains of aquatic calcareous organisms. We found diversified species of ostracods (*Ilyocypris inermis*, *Ilyocypris gibba*, *Candona neglecta* or *Fabaeformiscandona balatonica*...), gastropods (*Gyraulus* sp., *Valvata* aff. *piscinalis*, *Succineidae*...) and bivalves (*Pisidium* sp.), fish otoliths below 33 m, and algal remains (charophyte gyrogonites and calcified stems, *Phacotus* sp., *loricae*). All encountered biogenic taxa are typical of freshwater, shallow environments. These whitish units show a gradual transition at the base and passes abruptly to greenish silty clays at the top.

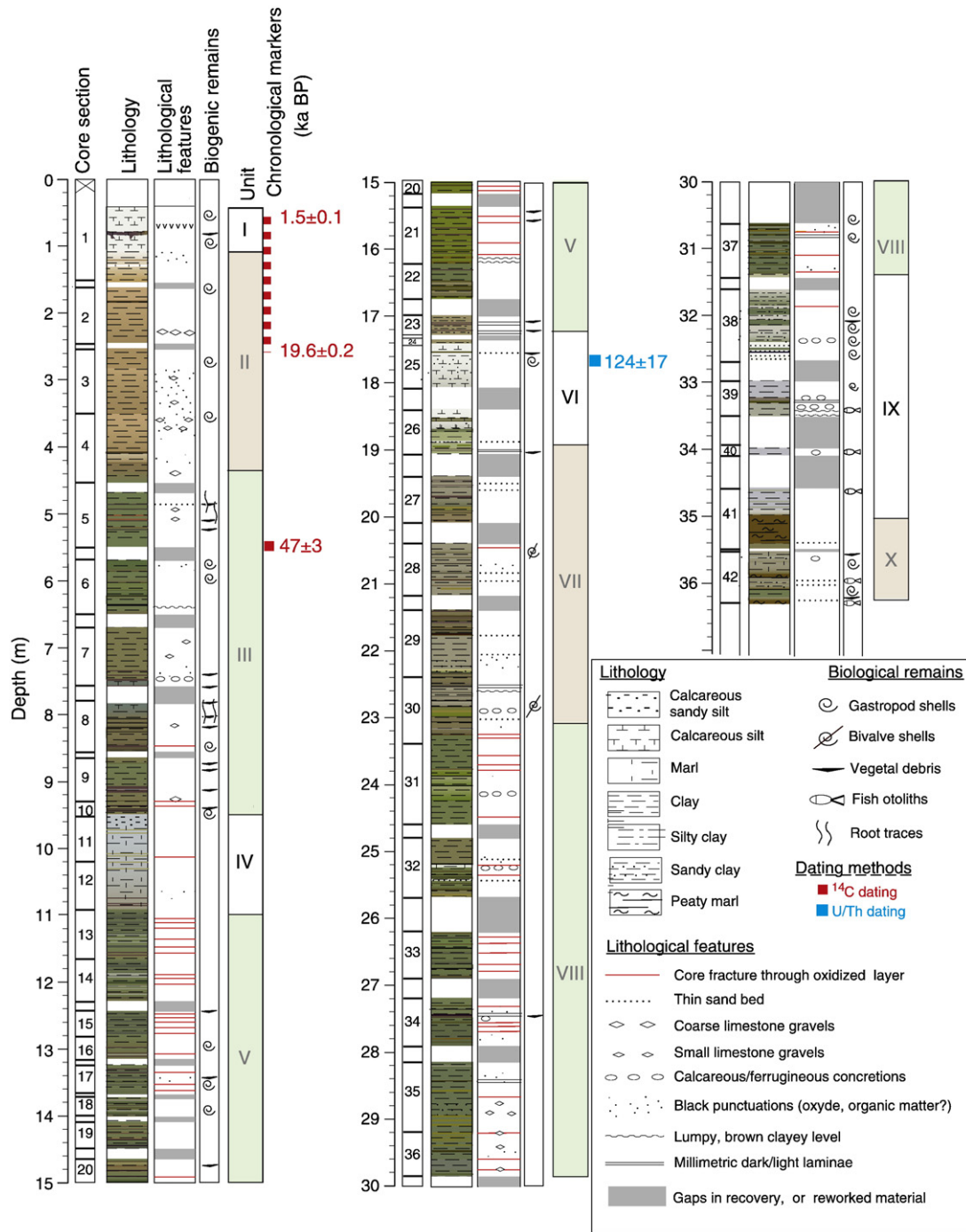


Fig. 3. Simplified stratigraphical log of YAM04C'. The gaps between sections are due to coring problems (lost of sediments at the base of core sections, or no sediment recovery). Rectangles: levels with radiocarbon (red) and U/Th (blue) ages. See lithofacies details in Appendix A.

Between these carbonate-rich units, darker clayey silts predominate. Units III, V, VII and VIII consist of finely banded olive gray or brownish gray clayey silts, almost devoid of aquatic faunal and algal remains, besides ostracods sometimes abundant but poorly diversified (*Ilyocypris* spp.). Layers rich in plant debris are frequent and generally form very dark millimetric beds interbedded in coloured silty clays. Some thicker dark bands (a few cm thick) show a lumpy texture and evoke paleosoils. Millimetric dark-light laminae occur occasionally. Limestones gravels and calcareous or ferruginous concretions are often organized in beds. Unit X is a peaty marl rich in fish rests and suggesting an accumulation of hydrophytes fragments in a productive marl. Unit II contrasts from others by its

reddish brown to ocher colour. This unit shows numerous strongly oxidized and indurated beds which suggest desiccation phases, and coarse limestone gravels.

U-channel sections collected along the entire core were used for paleomagnetic and X-Ray Fluorescence (XRF) scanner measurements at a resolution of 1 cm. Discrete samples were taken for other sedimentological analyses at variable intervals (from 2 to 15 cm) according to the main lithological features. In the watershed, 3 bedrocks and 4 soil samples (Fig. 2a) were collected for the characterization of the runoff-derived detrital fraction that has contributed to the lake sedimentation. Analyses were performed at CEREGE, otherwise it is specified in the text.

3.2. Major components of core sediments

3.2.1. Mineral composition

X-Ray Diffractometry (XRD) analyses were performed on core sediments (160 samples) and on watershed samples for a semi-quantitative estimate of the major mineral phases. Samples were dried and crushed in an agate mortar. The powder was sprinkled with a 100 μm sieve on circular silicon slides of 3 cm in diameter, in order to obtain a deposit of about 0.5 mm of thickness. Note that, in our analyses of bulk sediments, the relative proportions of clay minerals may be underestimated when mixed with well-crystallized grains, e.g., quartz or calcite.

The mineral composition of the clay fraction was analyzed for 8 levels from different stratigraphical core units (at 66, 400, 782, 963, 1506, 1761, 2634 and 3246 cm). Bulk samples were disaggregated by means of a 5–10% H_2O_2 solution. Carbonate was removed by 10% HCl. The suspensions were mounted as texturally oriented aggregates and solvated with ethylene–glycol vapor at a temperature of 50 °C.

All XRD analyses were performed on a Philips PW 1729 X-Ray diffractometer with a cobalt tube at 40 mA–40 kV.

Measurements of carbonate and organic matter contents were conducted on the same core sample set as for XRD (160 samples). Carbonate concentrations were obtained using a «Dietrich-Frühling» calcimeter. The method is based on the measurement of the CO_2 volume released during the reaction of the sediment with acid. The total carbonate content is calculated taking into account pressure, temperature, the sample weight, and the volume of released CO_2 . Contents in total organic matter (TOM) were estimated by loss on ignition (Dean, 1974) (weight lost of dry sediment by heating 2 h at 550 °C).

3.2.2. Element composition

The relative contents of major elements were measured by X-Ray Fluorescence (XRF) analyses. Measurements were performed every 1 cm on the core U-channels, using a XRF Avaatech core scanner (University of Bordeaux I, EPOC Laboratory). X-Ray beam was generated with a rhodium anode and a 125 μm beryllium window which allow voltage range of 7 to 50 kV and a current range 0 to 2 mA. The analytical settings were adjusted at 10 kV–400 μA in order to detect Ca, Si, Ti, Al, K, Mn and Fe. Each individual power spectrum was transformed by deconvolution process into relative contents (intensities) expressed in counts per seconds (cps). Element ratios (Si/Al, K/Al) could be used as indicators of the particle source and transport and weathering intensity (Zabel et al., 2001; Croudace et al., 2006).

3.2.3. Principal component analysis

Principal component analysis (PCA) was performed on the two sets of variables resulting from XRD and XRF analyses, using the R statistical software package (Ihaka and Gentleman, 1996; version 2.7.2). The goal was to reduce the number of observed variables to a smaller number of factors, providing insight into the structure of the variance of the parameters and to identify which set of variables form coherent subsets that are relatively independent of each another. Variables that are correlated with one another and which are largely independent of other subsets of variables are combined into factors. Factors were then related to the underlying sedimentary processes recorded in the sediments.

3.2.4. Sedimentary magnetism and paleomagnetism

Magnetic properties were used to trace surface erosion processes in the watershed (Thompson et al., 1980; Thompson and Oldfield, 1986). The low field magnetic susceptibility κ_{LF} , was measured on U-channels at 2 cm interval on the MS2C loop sensor connected to the Bartington susceptibility meter MS2. The natural, anhysteretic and isothermal remanent magnetizations (NRM, ARM, and IRM, respectively) were measured on a pass-through superconducting rock

magnetometer (2G model 760R) and demagnetized in alternating fields (AF) up to 60 mT using the on-line degaussing coil system. The ARM was imparted after nearly complete demagnetization of the NRM, by applying a 80 mT AF and a 50 μT steady field along the z axis of U-channels ($\text{ARM}_{0.05}^{80}$) and then stepwise AF demagnetized up to 60 mT. The IRM was imparted by passing U-channels through permanent magnets (Halbach cylinders) developing a 1 T transverse field (Rochette et al., 2001).

The low field susceptibility κ_{LF} , is primarily determined by the concentration of ferromagnetic (*s.l.*) minerals, but secondarily influenced by paramagnetic minerals (weak positive κ_{LF}) and by diamagnetic minerals (weak negative κ_{LF}). The $\text{ARM}_{0.05}^{80}$ is mainly carried by ferromagnetic (*s.l.*) minerals of low coercivity (e.g. the magnetite – Ti-magnetite series). The $\text{IRM}_{1\text{T}}$ includes contributions of higher coercivity minerals (hematite, goethite and iron sulfides). For a given concentration of ferrimagnetic minerals, all three parameters are grain size dependent: κ_{LF} and IRM are generally increasing with increasing grain size, while ARM is decreasing with increasing grain size.

Paleomagnetic tests were first performed on carbonate-rich and clayey-silty samples. Stepwise AF demagnetization diagrams exhibit remarkably stable direction up to 60 mT (demagnetization diagrams; Appendix B). The median destructive field (MDF) of the NRM ranges from 12 to 30 mT; and the 40 mT AF step leaves 15 to 40% of the initial NRM (Appendix B). The 35 mT demagnetization step was therefore selected to reconstruct profiles of inclination variations (declination profiles are hampered by coring artefacts). Intensities of the $\text{ARM}_{35\text{mT}}$ and $\text{IRM}_{1\text{T}}$ were taken as appropriate normalizers of the $\text{NRM}_{35\text{mT}}$ in order to reconstruct profiles of the relative paleointensity of the geomagnetic field, RPI (Johnson et al., 1975; Lund and Banerjee, 1979; Tauxe, 1993).

In order to trace sedimentary fabric disturbances, the anisotropy of the magnetic susceptibility (AMS) was measured on standard paleomagnetic cubic specimens extracted from layers characterized by anomalous NRM inclination, using a Kappabridge MFK1 magnetic susceptibility meter (AGICO). The orientation of the AMS ellipsoid, characterized by 3 orthogonal axes K_{min} , K_{int} and K_{max} , follows the statistical orientation of shape anisotropic magnetic grains and therefore characterizes the sedimentary fabric (Stacey et al., 1960; Hrouda, 1982; Martin-Hernandez et al., 2004). Namely, an oblate ellipsoid with a K_{min} axis vertical (90°) is typical for compacted sedimentary fabric. Significant deviations of this axis reflect sedimentary disturbances (e.g. slumps, sampling disturbances) potentially associated with anomalous paleomagnetic directions.

3.2.5. Additional analyses on discrete samples

In addition to routine smear slides observations along the whole sequence, selected carbonate-rich (66, 1048, 1770, and 3264 cm) and silty-clayey samples (750 and 815 cm) were observed in detail using a Nikon 50i polarizing optical microscope and a Hitachi S3000 Scanning Electron Microscope (SEM).

Grain size analysis was performed on core sediments from depth intervals covering transitions between stratigraphical units, and sampled every 15 cm between 45 and 200 cm (Unit II/I), 870–1020 cm (Unit IV/III), 1700–1900 cm (Unit VI/V) and 3060–3340 cm (Unit IX/VIII). Measurements were first performed on total sediment, then on samples decarbonated with 10% HCl. We used a Malvern Mastersizer S laser diffractometer and three successive measurements were systematically performed for each sample. The Malvern software provides a size spectrum ranging from 0.06 μm to 878.67 μm .

The stable isotopic composition of carbonates from the watershed and core sediment samples was measured in order to differentiate two end-members, detrital carbonates (derived from clastic inputs), and authigenic carbonates (precipitated in the lake), through their respective isotopic signatures. Analyses were performed on 7 samples from the watershed (soils and bedrock; Fig. 2a) representative of the

detrital end-member, and on 4 calcite-dominated core samples (taken at 66, 1767, 3264 and 3406 cm). For core samples, measurements were conducted on both bulk material and different size fractions (<25 µm, 25–63 µm and 63–150 µm), and on the best preserved *in situ* ostracod valves taken from the fraction >150 µm. Ostracod values were corrected for vital effect (Develle et al., 2010) to obtain values coeval of authigenic calcite precipitated at equilibrium in the lake water (authigenic end-member). The determination of the carbonate $\delta^{18}\text{O}$ and $\delta^{13}\text{C}$ values was performed on CO_2 resulting from the reaction of the carbonate with H_3PO_4 acid at 70 °C, with a Finnigan Delta Advantage mass spectrometer. Analytical precision of $\delta^{18}\text{O}$ and $\delta^{13}\text{C}$ is $\pm 0.04\%$ and $\pm 0.02\%$, respectively, based on repeated analyses of a NBS-19 limestone standard (-2.2% and $+1.95\%$ for $\delta^{18}\text{O}$ and $\delta^{13}\text{C}$, respectively).

3.2.6. Age assessment

The chronology of the upper 535 cm of the core was established by ^{14}C dating. Below this depth, the U/Th disequilibrium dating method was attempted on bulk samples or size fractions of core sediments containing $\geq 80\%$ of calcite. In addition to radiometric dating, paleomagnetism has been used to provide additional control on the age model.

4. Results

4.1. Sedimentological analyses

We first consider the results from the bedrock and soil samples collected in the watershed for understanding the contribution of local detrital inputs (including carbonates) to the paleolake sedimentation. We then characterized the typical carbonate-rich and siliciclastic intervals observed in the sediment core.

4.1.1. Bedrock and soils from the Yammoûneh watershed

The local bedrock mainly consists of calcite. The mineral assemblages of soil samples are mainly composed of three major mineral phases: calcite, quartz and clay minerals (mainly smectite and kaolinite) in varying proportions. For example, YamSol3 and Ainata samples contain 50% of calcite, 30% of quartz and 20% of clay minerals (hereafter, all percentages are given as dry sediment weight %); YamSol2 shows a lower calcite content (7%) and higher percentages of quartz (~60%) and clay minerals (~33%). In soil samples, microscopic observations show calcite grains occurring mostly as aggregates, and eroded round and matt quartz grains (<20–50 µm) associated with iron oxides filling surface dissolution cavities.

4.1.2. Core sediments

Major sedimentological results on core YAM04-C' are illustrated in Figs. 4 to 8. Calcimetry and XRD (Fig. 4), and XRF intensities (Fig. 5) show that the carbonate fraction is important all along the sequence, mainly represented by calcite. All variables show significant variations within individual stratigraphical units and gradual transitions between some of them (especially from Units VII to VI and Units III–II to I). Nevertheless, carbonates clearly predominate in Units I, IV, VI and IX, whereas siliciclastic components prevail in clayey-silty Units II, III, VII and VIII.

As expected in a karstic basin with rapid throughflow, sediment components throughout the sequence indicate freshwater conditions in the Yammoûneh waterbody. This agrees with biological remains which also reflect shallow or even sub-aquatic biotopes.

4.1.3. Main characteristics of the carbonate component

In carbonate-rich Units I, IV, VI and IX, calcite represents more than 70% of the sediment and up to 85–100% in Units I, VI and IX (Fig. 4). The very low aragonite contents in layers rich in mollusc shells or fish otoliths suggest recrystallization of this unstable mineral in calcite. TOM content reaches its minimum values (2–5%; Fig. 4). Magnetic

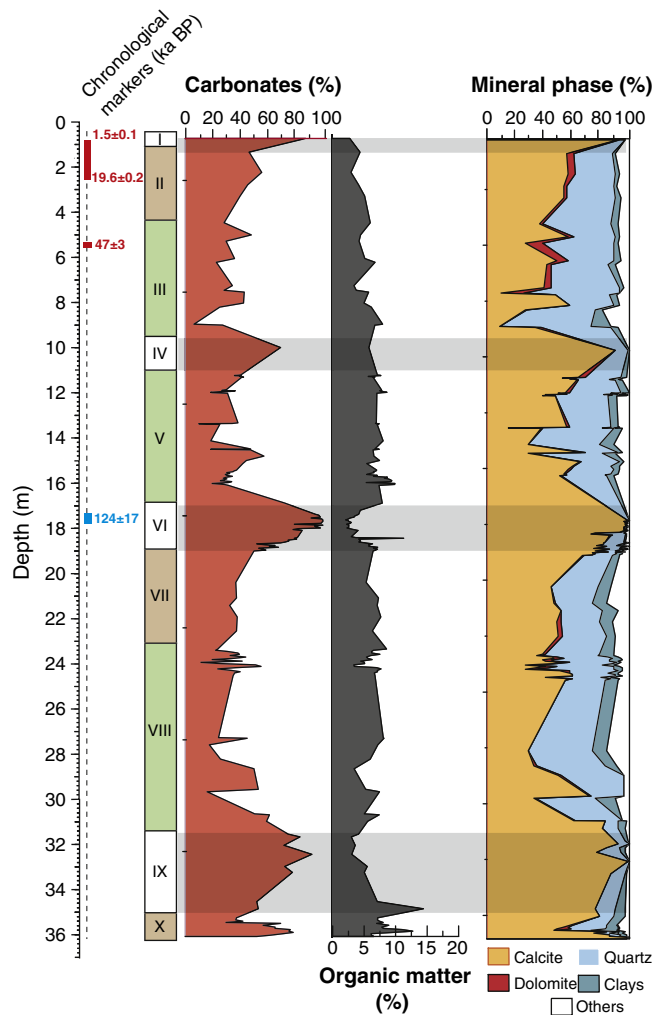


Fig. 4. Major components of the Yammoûneh core sediments: carbonate content (calcimétrie), organic matter contents (loss on ignition) and major mineral phases (XRD analysis). Rectangles indicate stratigraphical position of ^{14}C (red) and U/Th (blue) ages.

susceptibility is low and/or negative and low ARM intensities ($< 0.5 \cdot 10^{-1} \text{ A} \cdot \text{m}^{-1}$, Fig. 5) confirm the weak concentration of ferromagnetic particles probably due to the strong dilution by carbonates. Grain size analysis of bulk sediments shows a multimodal particle distribution dominated by sand-size particles (not shown). SEM observations reveal abundant rhomboedric calcite crystals (authigenic) up to 30 µm long (Plate Ia). The coarser particles include calcitic rests of aquatic organisms and algal precipitation (Plate Ib, c), but also carbonate aggregates (Plate Ie) which might have derived from the bedrock erosion or soil reworking. Stable isotope measurements performed on 4 core samples (bulk and different size fractions) retrieved in carbonate intervals (Units I, VI, and IX) show $\delta^{18}\text{O}$ values of ca -9 to -11% and $\delta^{13}\text{C}$ values ranging from -2 to -6% . When plotted on a $\delta^{18}\text{O}$ versus $\delta^{13}\text{C}$ diagram (Fig. 6), these values are significantly lower than isotope values of the watershed samples indicator of the detrital carbonate end-member, and close to those of ostracod valves retrieved from the same samples (once corrected from the vital effect), regarded as representative of the authigenic calcite end-member. These results suggest that carbonated units mainly consist of authigenic calcite, but a minor contribution of detrital calcite and of recrystallized aragonite cannot be excluded.

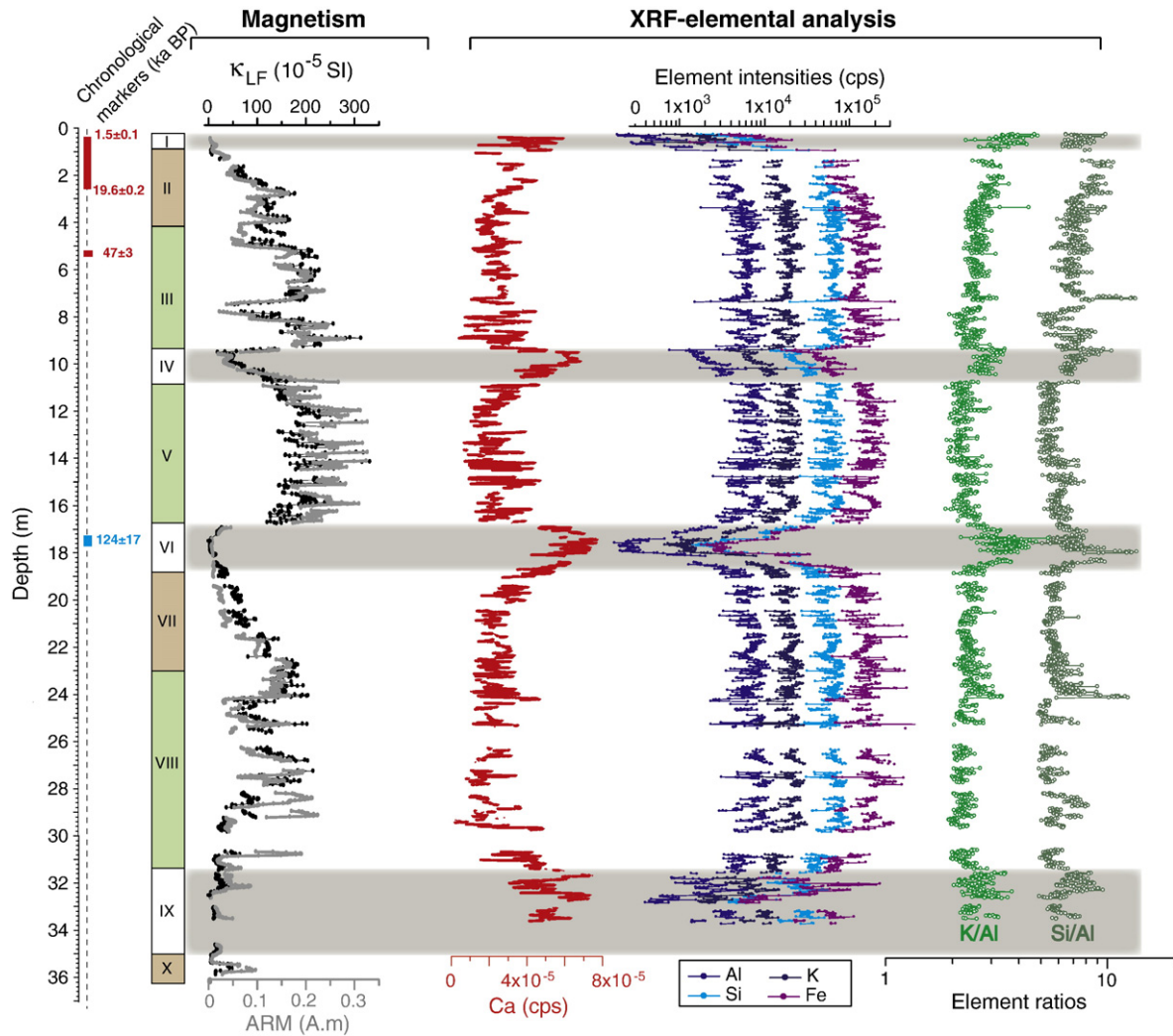


Fig. 5. Down-core sedimentological variations based on: concentration in magnetic particles (κ_{LF} , ARM), major element intensities and element ratios (Si/Al, representing quartz versus other silico-clastic minerals, and K/Al, indicator of catchment weathering or of wind-blown K-rich minerals).

Relatively high carbonate contents (7–55%) are also present in the silty-clayey units (as defined in Section 3.1) and mainly consist of calcite in the form of rounded aggregates or limestone gravels. In these units, calcite rhomboedric crystals and biogenic calcified remains

are rare, although some levels are relatively rich in calcite and in ostracod valves.

4.1.4. Main characteristics of the clayey-silty components

XRF relative abundances of Si, Al, K and Fe roughly mirror Ca-intensities and reach their maximum values (Fig. 5) in stratigraphical Units II, III, V and VIII. These units are characterized by high contents of quartz associated with silicate minerals in lower amounts, and mixed with carbonates. Quartz contents vary around 30% and reach 60% in Unit III (Fig. 4). Quartz grains are round and matt, with a size of 20 μm in average but may reach 50 μm , and closely resemble those from the watershed samples (altered, partly dissolved and intimately mixed with iron oxides; Plate If). Angular K-feldspars and plagioclases crystals have approximately the same size but are better preserved (Plate Id). TOM content is >5% and peaks at 15% in the peaty marls at the Units IX–X transition (Fig. 4). The clay fraction is composed of smectite (60–70%), kaolinite (25–30%) and a few percents of illite. Low amounts of dolomite occur by times. Downcore variations in magnetic particles concentrations, recorded by the magnetic susceptibility (κ_{LF}) and ARM (Fig. 5), run parallel to those of siliciclastic elements and minerals. High κ_{LF} and ARM values are associated with high amount of ferrimagnetic particles. The high amplitude of proxy variations between carbonated and clayey-silty layers is partly due to dilution by contribution of carbonates. Nevertheless, other processes, like changes in mineralogy assemblage linked to a change in detrital sources and/or early diagenesis processes

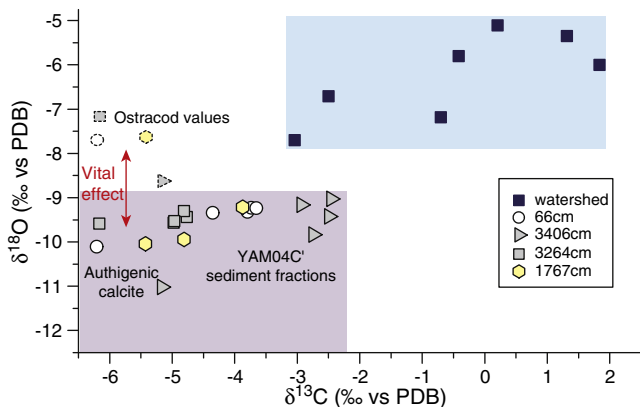


Fig. 6. Isotopic composition ($\delta^{18}\text{O}$, $\delta^{13}\text{C}$) of bedrock and soil samples collected in the watershed (blue symbols), and of carbonate-rich lacustrine deposits from YAM04C' (black, gray and white symbols). $\delta^{18}\text{O}$ values of authigenic calcite are estimated from the $\delta^{18}\text{O}$ of ostracod valves corrected from the vital effect.

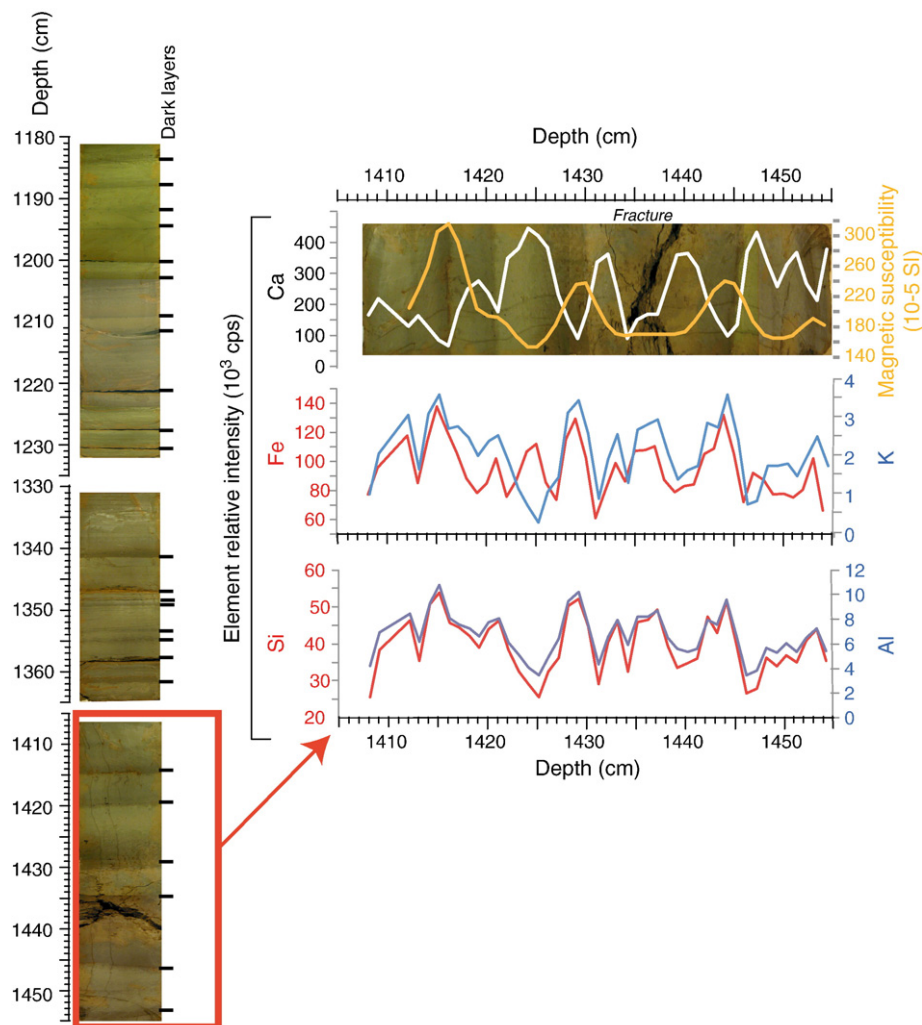


Fig. 7. Short-term sedimentary changes in silty-clayey deposits. Example of changes in magnetic susceptibility and element intensities in the interval 1180–1455 cm (Unit V).

may be also responsible for these variations. Interestingly, the element ratios Si/Al and K/Al (Fig. 5) reveal peaks occurring within the carbonate-rich units suggesting that the reduced detrital fraction in these intervals is mainly composed of quartz and K-feldspars (Fig. 5). Whatever the unit, grain size analysis of decarbonated samples show a well sorted silt-size peak with one mode centred at 15 μm .

The clay-silt units are far from being homogeneous. High frequency variability in sedimentary conditions is particularly clear in the occurrence of finely banded greenish intervals. As an example, Fig. 7 illustrates the fluctuations of K_{LF} and element intensities (Ca, Si, Al, K and Fe) in the interval 1100–1650 cm (Unit V), in agreement with subtle changes in colour, grain size and content in plant debris which decrease from the base to the top of individual bands. However, the discussion will be focused on long-term changes in the sedimentary components.

4.1.5. PCA-results

Main sedimentary features of these two types of sediments are synthesized using PCAs. The sampling resolution differs depending on the analysis. We thus performed individual PCAs for XRD and XRF (hereafter noted PCA_{XRD} and PCA_{XRF} ; Fig. 8), and then compared their outputs. Only factors having Eigen-values >1 or just below 1 are considered. Factors 1 and 2 are noted F1 and F2. In PCA_{XRD} , two factors explain 62% of the total variance. F1XRD (37% of the total variance) is dominated by high contribution of quartz and moderate loadings of feldspars, clays and dolomite (Fig. 8b). These components are

negatively correlated to calcite and aragonite. F2XRD (25% of total variance) is positively correlated with clays. In PCA_{XRF} , F1XRF (78% of total variance) is mainly explained by the high positive loading of calcium which is negatively correlated to all other elements (Fig. 8b). The first component projections of these PCAs (Fig. 8) highlight the antiphasing between calcite and aragonite which are partly authigenic, and typical detrital components derived by runoff from the watershed or wind-transported to the lake (quartz, clays, feldspars, dolomite, Si, Ti, Al, K, and Fe).

4.2. Chronological framework

The ages proposed subsequently are related to Marine Isotope Stages (MIS) as defined by Martinson et al. (1987).

4.2.1. Radiometric dating

The chronology of the upper 535 cm of the core was established by ^{14}C dating of partially carbonized wood fragments, relatively abundant in the trenches but rare in the core. The age model for the last 21,000 years (*ca* 250 cm in the core YAM04C') has already been established using 12 calibrated ^{14}C ages from the 2 trenches (Daëron et al., 2007, and pers. comm.) and from the core. The core-trench stratigraphic correlation was based on remarkable lithofacies, magnetic susceptibility, oxygen isotope records and ^{14}C dates (Develle et al., 2010). An additional ^{14}C age was obtained at 535 cm in the core.

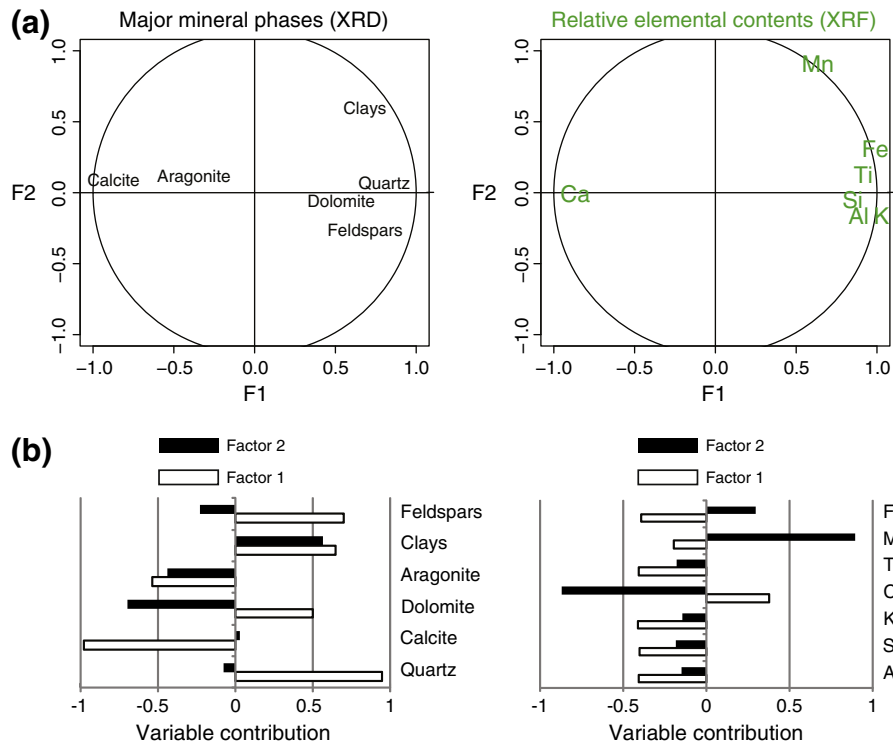


Fig. 8. Principal Component Analyses (PCAs) of major sedimentological data. (a) PCA F1/F2 projection of variables scores in PCA-XRD, PCA-XRF. (b) Contribution of the variables and their association with the factors F1 (white) and F2 (black).

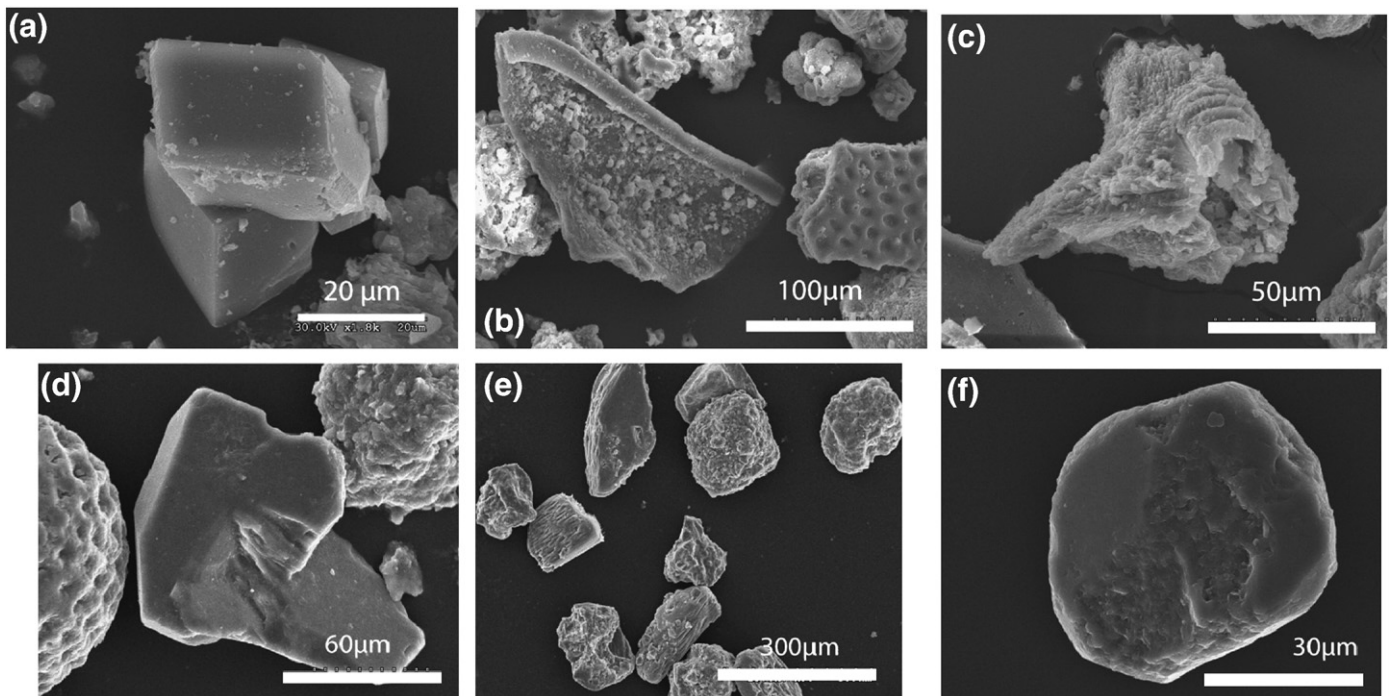


Plate I. SEM pictures of the major particles and minerals identified in the YAM04C' core.

- (a). romboedric calcite grains,
- (b). ostracod rests,
- (c). algal precipitations,
- (d). K-feldspars,
- (e). calcite aggregates and quartz grain.
- (f). quartz grain.

According to available ^{14}C dates, Unit I represents the Holocene period (MIS 1), truncated in the core at about 6 ka likely due to plowing; Unit II includes the lateglacial, the Last Glacial Maximum (LGM), and possibly part of MIS 3. The ^{14}C age of 47 ± 3 ka (535 cm) also places the top of Unit 3 in MIS 3. This age should be regarded with caution as it reaches the limit of the radiocarbon dating method applicability.

Below 535 cm, an attempt was made to apply the U/Th disequilibrium dating method. U-series analyses were performed on bulk samples or size fractions of core sediments containing $\geq 80\%$ of calcite. Most samples appear unsuitable for U/Th dating for mainly three reasons: (i) a too high contamination by detrital fraction, highlighted by high ^{232}Th values (Table 1) and also detrital carbonate from the drainage basin; (ii) multiple sources of detrital carbonate supplies (e.g., watershed and wind-blown particles of unknown origin); (iii) the system did not remain closed. Only one level (1770 cm; Unit VI; calcite content close to 100%) has provided apparently acceptable results from TIMS measurements and yields an uncorrected age of 139.6 ± 13.4 ka (Table 1). However, the measured $^{230}\text{Th}/^{232}\text{Th}$ ratio (5.8 ± 0.3) indicates that this initial age is too old and should be corrected for the contribution of a detrital fraction by using the detrital $^{230}\text{Th}/^{232}\text{Th}$ ratio, which is unknown at Yammoûneh. One way to estimate the detrital fraction is to use the isochron methods. Using an Holocene sample dated at 5.5 ka in the trench TR02, this tentative failed (U/Th age 12 ka older than the ^{14}C age) likely due to a mixture of carbonate detrital particles from several sources. Another way is the analysis of pure detrital material. Analyses (α -counting) of two carbonate-poor layers of the core (1696 and 4100 cm, dominated by clay and plant debris) suggest a detrital $^{230}\text{Th}/^{232}\text{Th}$ ratio ranging between 0.8 and 1.9 (not shown), consistent with the values most commonly found in the literature. Taking theoretical detrital $^{230}\text{Th}/^{232}\text{Th}$ ratios of 0.63, 1, 1.3 and 1.7 for correction (Kaufman, 1993 and references therein), re-calculated ages (mean: 124 ± 17 ka) fall within the last interglacial maximum, the MIS 5–5 (Eemian) whatever the ratio used (Table 1 and Appendix C). Despite large uncertainties, stratigraphical Unit VI, which closely resembles the Holocene, can be assigned to MIS 5–5.

4.2.2. Magnetostratigraphy

Along the sequence, normal inclination values of the $\text{NRM}_{35\text{mT}}$ in YAM04C' samples oscillate between 40° and 60° (Fig. 9a), in conformity with the record of a paleomagnetic secular variation, as reconstructed from other late Pleistocene sequences studied in northern mid-latitude sites. The average inclination (51°) is consistent with the inclination of the field vector generated at the site latitude (34°N) by a geocentric axial dipole.

Variations of the relative paleointensity (RPI) of the geomagnetic field were reconstructed using the $\text{NRM}_{35\text{mT}}/\text{ARM}_{35\text{mT}}$ and $\text{NRM}_{35\text{mT}}/\text{IRM}_{1\text{T}}$ ratios profiles (Fig. 9b and c). These are essentially similar, although the $\text{NRM}_{35\text{mT}}/\text{ARM}_{35\text{mT}}$ ratio exhibits two unexplained spikes in the upper parts of intervals VII and VIII. In Fig. 9d, the PISO 1500 stack based on marine cores (Channell et al., 2009) and the regional RPI-stack from the Portuguese margin (Thouveny et al., 2004) are plotted as global and regional reference records.

Table 1
Uranium and thorium concentration measured in the Yammoûneh sample at 1770 cm. Uncorrected and corrected ages based on $^{230}\text{Th}/^{232}\text{Th}$ ratios the most commonly used in the literature (Kaufman, 1993).

^{238}U (ppb)	^{232}Th (ppb)	$^{234}\text{U}/^{238}\text{U}$	$^{230}\text{Th}/^{234}\text{U}$	$^{230}\text{Th}/^{232}\text{Th}$	Detrital $^{230}\text{Th}/^{232}\text{Th}$ (*)	Age uncorrected (ka BP)	Age corrected (ka BP)
411.74 ± 2.31	279.52 ± 3.32	1.66 ± 0.01	0.77 ± 0.03	5.8 ± 0.2	0	139 ± 13.4	
					0.63		131.6 ± 12.3
					1		126.5 ± 11.7
					1.3		122.2 ± 11.2
					1.7		116.1 ± 10.5
Sample age							124 ± 17

(*) Theoretical detrital $^{230}\text{Th}/^{232}\text{Th}$ using the most common values used in the literature (see Kaufman, 1993 for details).

Below the ^{14}C -dated section of the core, four depth intervals (noted 1 to 4) present low or negative inclination values. Three of these anomalies correspond to low RPI values documenting events of low dipole field. These intervals (Fig. 9) can thus be interpreted as records of geomagnetic excursions. This allows us some chronological anchor points to be proposed along the 36 m sequence.

Interval 1 (340–370 cm, clayey silt Unit II) is marked by a RPI low and inclination deviation of $\sim 40^\circ$, centred at 365 cm. It likely coincides with the Laschamp event, dated at 40.4 ± 1.1 ka by $^{40}\text{Ar}/^{39}\text{Ar}$ dating at the “Puy de Laschamp” (Guillou et al., 2004). An age of $\sim 41 \pm 1$ ka is attributed to Interval 1, in relatively good consistency with the bracketing ^{14}C ages. Interval 2 (1590–1660 cm, clayey silty, Unit V) is characterized by a sharp negative inclination peak at 1610 cm. The same signal was also recorded in core YAM04C' (not shown) collected few meters apart YAM04C'. This large deviation is attributed to the Blake geomagnetic event recorded at 115–120 ka BP in the PISO and Portuguese margin stacks. This event was dated between 114 and 120 in Chinese loesses (Fang et al., 1997). We adopt an age range of 114–120 ka for Interval 2, in stratigraphical agreement with the Eemian age obtained from U/Th dating for the underlying Unit VI.

The excursions behaviour of the paleomagnetic signal in the Yammoûneh section corresponding to the Blake event is remarkable. To confirm this signal and to rule out possible sedimentary disturbances, we measured the anisotropy of magnetic susceptibility (Appendix B). The magnetic fabric is characterized by a short axis K_{min} of the magnetic ellipsoid close to vertical (90°) imaging a non-deformed sedimentary fabric confirming the validity of this signal.

Below 1800 cm, the geomagnetic signals are less clear partly due to gaps in the core sediment recovery. The RPI and inclination deviations centred at ~ 2735 cm (Interval 3; clayey silt Unit VIII) may reflect the Iceland Basin event placed at 190–194 ka in marine records (Thouveny et al., 2004; Channell et al., 2009) and well identified in continental sites (e.g., Lake Baikal, Oda et al., 2002; Demory et al., 2005b). The negative inclination deviation around 3460 cm may coincide either with the Pringle Falls excursion (~ 211 ka; Herrero-Bervera et al., 1994; Channell et al., 2009) or with the Mamaku excursion, dated at 230 ± 12 ka in lava flows of New Zealand (Shane et al., 1994). We consider the entire time interval 211–240 ka between these two excursions and attribute a mean age of 230 ka at Interval 4. Nevertheless, this part of the sequence suffers from (i) the lack of chronological constraints below 3460 cm and (ii) many gaps between sections. This part of the sequence has thus to be considered with caution.

4.2.3. Age model

Taking into account the 13 ^{14}C ages from the upper 535 cm, the U/Th date around 124 ± 17 ka at 1770 cm, and the four age control points based on paleomagnetic events (41 ka at ~ 365 cm; 114–120 ka around 1635 cm; ~ 190 ka at 2735 cm; ~ 230 ka at 3460 cm), the 36 m sequence of the YAM04C' core spans approximately 250 ka. We are not able at that stage to constrain changes in sedimentation rates between the few dated points, except an increase between Units II (ocher clayey silt) and I (powdery carbonate) in the upper 3 m. Furthermore, sedimentation hiatuses may have occurred, as identified during the early stages of

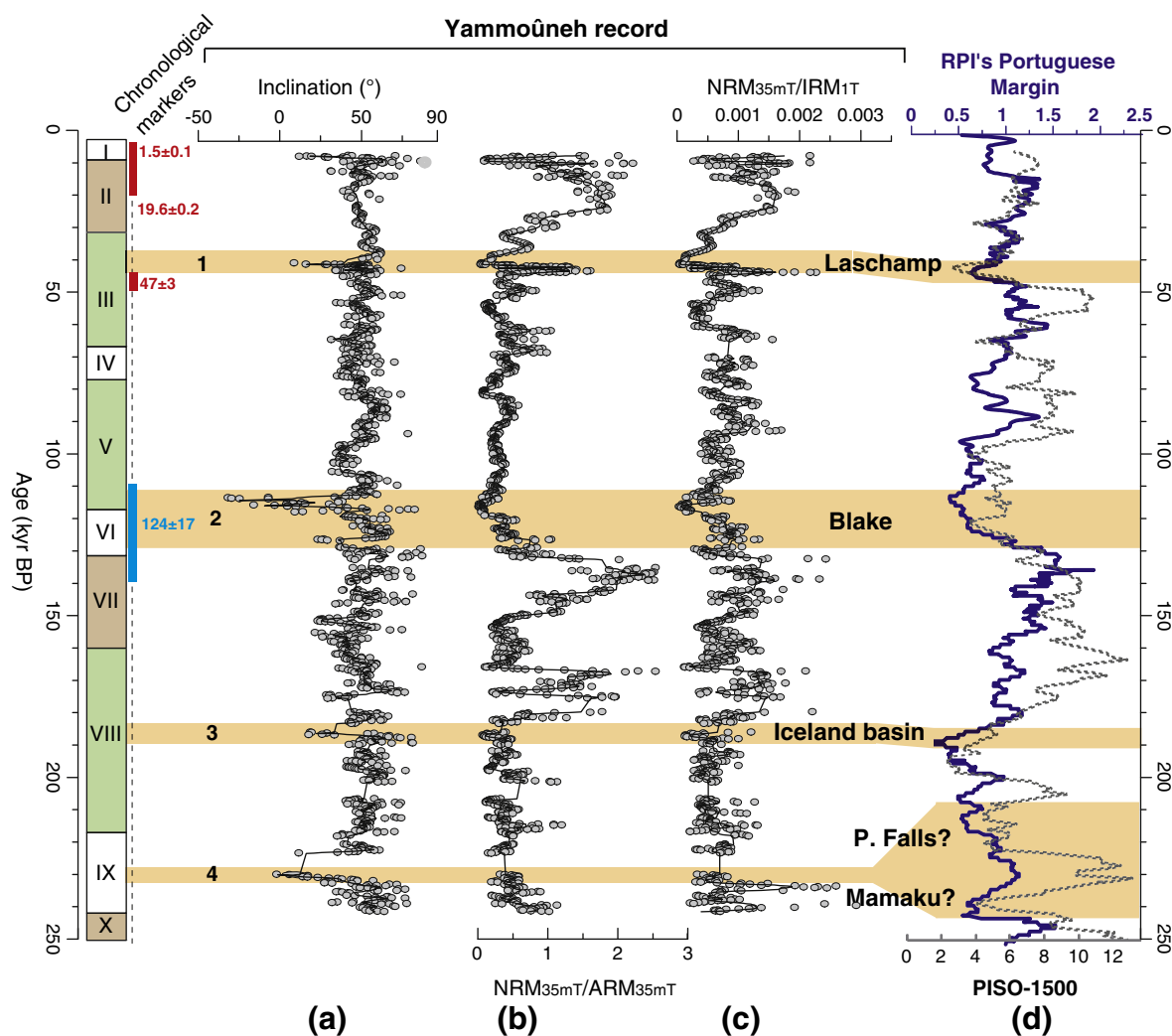


Fig. 9. Downcore variations in the magnetic parameters used for magnetostratigraphy along the 36 upper meters of the YAM04C' core. (a) Inclination. (b and c) RPIs (NRM normalized to ARM and IRM). (c) Comparison with the global stack PISO 1500 variations (Channell et al., 2009), and the Portuguese margin RPI record (Thouveny et al., 2004). Pink areas indicate correlations between magnetic events recorded at Yammouneh (1–4) and dated global excursions. Rectangles indicate stratigraphical position of ¹⁴C (red) and U/Th (blue) ages.

Termination I (Develle et al., 2010). Therefore, linear interpolations between dated points (Fig. 10), which themselves suffer significant chronological uncertainties, only provide an approximate timing of observed changes. Nevertheless, stratigraphical units I (early Holocene) and V can be assigned with confidence to interglacial stages MIS 1 and MIS 5.5, respectively. Assuming that the penultimate interglacial maximum is also recorded by carbonate-rich sediments (as Units I and VI) and that the mean sedimentation rate between the oldest ¹⁴C-dated level and the sequence base remains almost constant, Unit IX might represent MIS 7 (7–3 or 7–5?).

5. Discussion

5.1. Carbonate sedimentation during interglacial maximum

Units I, VI and IX, assigned to the interglacial periods MIS 1, MIS 5.5 and MIS 7, respectively, show a high proportion of calcite precipitated within the waterbody, in the form of romboedric calcite crystals and shells of aquatic organisms.

Inorganic calcite precipitation in freshwater bodies is favoured by: (i) photosynthesis activity of algae and aquatic macrophytes that consumes CO₂ and increases the water pH; (ii) increase in water temperature; (iii) water saturation with calcium (Bathurst, 1975;

Kelts and Hsü, 1978; Kelts and Talbot, 1990). Strong correlations between calcite precipitation, water temperature and primary productivity were demonstrated for example in Lake La Cruz (Spain; Romero et al., 2006). Open-water precipitation of calcite is common in hard water lakes which often undergo «whiting events» during summer months (Effler, 1987; Mullins, 1998). In karstic systems, springs represent a major source of Ca²⁺ ions derived from the dissolution of bedrock limestones that interact with meteoric water. This process is enhanced if water percolates through well-developed soils. Intense biological activity in soils (respiration and microbial activity) results in an excess of soil acidity, a pH decrease of percolating water and thus a more effective limestone dissolution. Carbonate preservation in lakes is positively related to water oxygenation (Dean, 1999). Water in shallow lakes is most commonly well-mixed and well oxygenated by wind-induced turbulence, while CaCO₃ precipitated in the epilimnion of deep stratified lakes is often dissolved in the hypolimnion where anoxic conditions cause the decomposition of organic matter and a reduction in water pH.

Favourable conditions for authigenic and biogenic carbonate production and preservation were clearly reached at Yammouneh during interglacial maxima (Fig. 11a). A good oxygenation through the water column is attested by the rich aquatic biocenose including a benthic fauna and the whitish colour of the sediments. Algal and fish

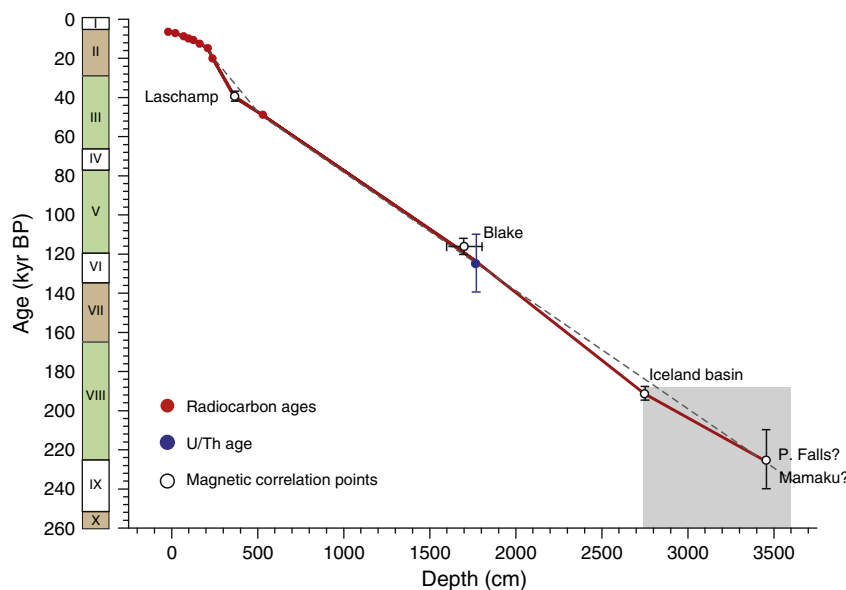


Fig. 10. Age versus depth diagram proposed for the upper 36 m of core YAM04C'. Black dashed line: preliminary age model based on ^{14}C ages and U/Th dating. Red line: age model based on ^{14}C ages, U/Th dating and magnetic events identified in the sequence. The gray area represents the part of the sequence which suffers from chronological uncertainties and has to be considered with caution.

rests suggest high productivity, despite low content in TOM possibly diluted by carbonates and/or oxidized through well ventilated conditions. High carbonate production implies high Ca^{2+} availability, suggesting an important discharge of karstic springs and an active water circulation in the Mnaïtra aquifer, and thus significant precipitation in its recharge zone (Fig. 12a). The low amount of clastic material indicates that detrital inputs from the watershed were either diluted by the lake carbonate production, or considerably reduced. Influx of siliciclastic material from the watershed might be minimized by a dense vegetation cover around the lake, or by local rains too low to drain particles from the basin slopes. Pollen data, illustrated here by the percentage ratio of arboreal versus non-arboreal pollen grains, AP/NAP (Fig. 11b) show that the development of arboreal taxa around the lake culminated in phase with maximum carbonate concentration. Catchment erosion was thus limited by the vegetation cover, and related soil development favoured the limestone dissolution in the surface and underground network (Fig. 12a). The tree growth was certainly favoured by the warm interglacial conditions, but also implies relatively high available moisture. We thus favour the hypothesis of wet conditions in both the aquifer recharge zone and in the Yammoûneh basin during interglacial periods.

We note that some of the Si/Al and K/Al ratios peak in the carbonate-rich units, especially around 128 ka. The Si/Al ratio (Fig. 11c) can be considered as a tracer of wind-blown quartz grains. High K/Al ratios may reflect weathering in the watershed, but the positive correlations between: (i) quartz and K-feldspars percentages in XRD analyses and (ii) K/Al and Si/Al ratios (despite small shifts between maximum values), rather indicate eolian influxes of K-rich minerals. The potential sources of windblown quartz and feldspar grains, much more abundant in silty clayey sediments, are discussed below. Their relative high abundance during periods of reduced soil erosion in the watershed suggests direct falls of eolian dust on the waterbody surface, in contrast with intervening periods.

By analogy with interglacial optimum (MIS 1, 5–5 and 7–3? or 7–5?), the carbonate-rich Unit IV is assumed to represent MIS 5–1, despite its higher detrital content (Fig. 4). If this is correct, the top of Unit IV would be a few k-years older than as suggested by our linear age interpolation. Slight increases in Ca content, K/Al, Si/Al and AP/NAP ratios around 15 m (~100–110 ka; Unit V) likely reflect MIS 5–3. We thus assume that the whole interglacial MIS 5 is represented by Units VI, V and IV (ca.

1865–950 cm). The finely banded clayey sediments of Unit V (Figs. 3 and 7) suggest repetitive surges of water loaded with detrital particles induced by rainfall events, and interrupted by wetter periods with enhanced tree growth and in situ carbonate production. The base of Unit VIII, which is relatively rich in calcite, might fit MIS 7–1.

5.2. Sedimentation during glacial periods: Watershed versus eolian inputs

The clear relationships between the mineral composition of the watershed soils and that of core sediments indicate that most of the siliciclastic elements are eroded from the surface catchment area and transported by runoff, although authigenic calcite (and possibly neogenic phyllosilicates) and local organic production may contribute to sedimentation by times.

Detrital calcite, dolomite and clay minerals may easily derive from the catchment bedrock weathering and erosion. Conversely, quartz, the dominant siliciclastic mineral, K-feldspars and plagioclases, absent from the basin bedrock, are obviously wind-blown from a remote source. The high quartz contents reflect the significant contribution of wind borne particles to glacial age sediments, by reworking of eolian dust from the basin soils and direct fall on the lake surface. Quartz likely comes from desertic areas from surrounding countries and the large Saharan–Arabian deserts. Saharan dust inputs to the Levantine basin (core ODP 667: Larrasoana et al., 2005; core SL112: Hamann et al., 2008) and in a speleothem from Jerusalem West Cave (Frumkin and Stein, 2004) have been related to the monsoon-modulated climate in the northern Sahara controlled by the precessional forcing. At Yammoûneh, quartz grains are generally too coarse to have been transported from such a distal source (Tsoar and Pye, 1987). Taking into account the quartz grain size and dominant synoptic systems bearing eolian dust (Cyprus low and to a lesser extent Sharav cyclone and Red Sea trough; Dayan et al., 2008), two potential sources can be proposed: (1) the late Pleistocene loess of the Negev desert (~300 km southward) dominated by quartz grains 50–60 μm large, themselves derived from Sinai–Western Negev sand dunes (Crouvi et al., 2008), and sorted through eolian abrasion and transport to Yammoûneh; (2) the exposed Mediterranean shelf when the global sea-level was approx. 100–120 m below the current sea level, exposing the shallow shelf off the northern Sinai coast during glacial stages (Enzel et al., 2008.). K-feldspars and plagioclases may

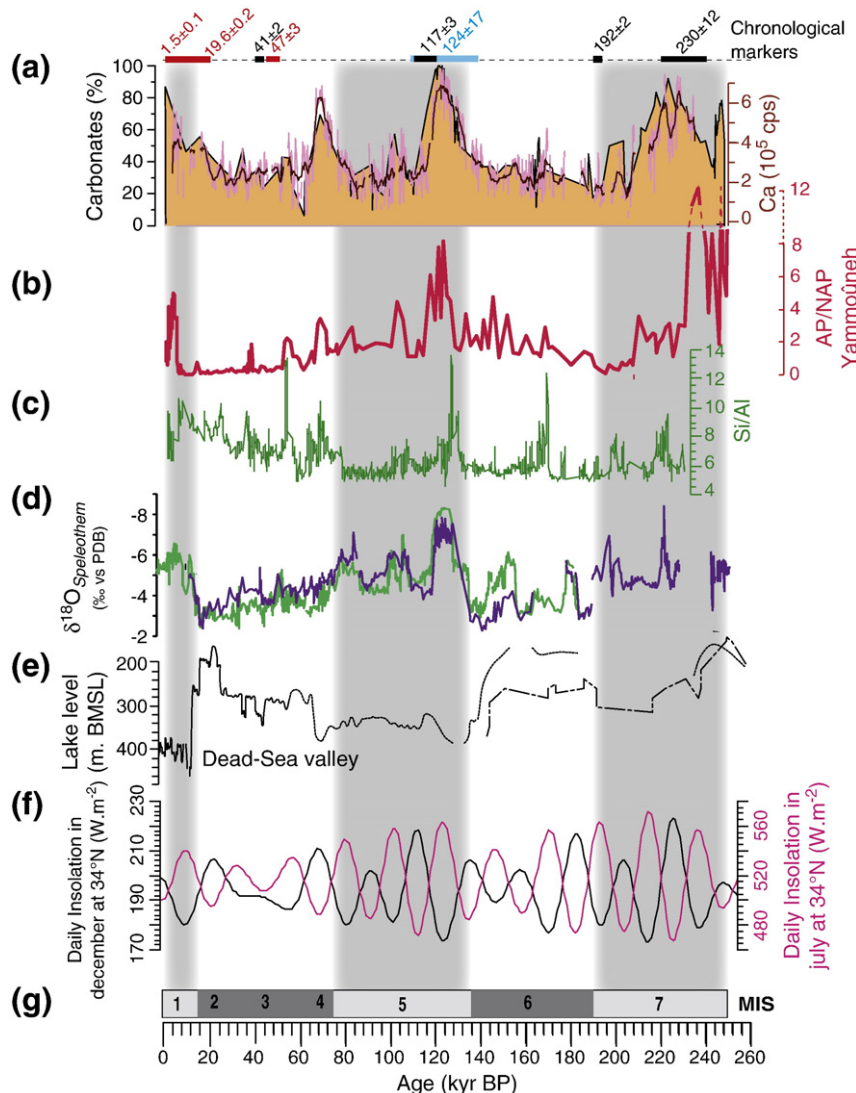


Fig. 11. Downcore variations of some proxies from Yammoûneh as a function of age: (a) carbonate contents and Ca intensities, (b) AP/NAP ratio and (c) Si/Al ratio. Comparison with some key paleoclimatic records from the Levant over the last 250 ka. (d) Soreq and Peqin cave isotopic records and (e) lakes of the Dead Sea Basin (see Fig. 1 for references), (f) seasonal insolation parameters at 34°N and (g) age of sapropel events in Eastern Mediterranean (Emeis et al., 2003) and Marine Isotopic Stages according to SPECMAP (Imbrie et al., 1984).

have the same origin, but their good preservation suggests a more proximal source (i.e., Mesozoic and Cenozoic basalts outcropping in central and northern Lebanon, respectively) (Abdel-Rahman, 2002; Abdel-Rahman and Nassar, 2004).

In Units VIII, VII (MIS 6) and III (MIS 4 and early MIS 3), accumulations of greenish-brownish clayey silts imply local weathering and runoff, and thus rains or melt-water surges in the basin. Although the AP/NAP ratio is lower than during the interglacial optimum, relatively developed arboreal vegetation and abundant plant debris indicate some vegetation growth on the surrounding slopes or the basin floor. Efficient moisture may be enhanced by low evaporation rate under glacial thermal conditions. However, local water availability was too low to allow the development of a diversified aquatic biocenose. The single ostracod specie (*Ilyocypris inermis*) well survives ephemeral waterbodies. Several layers suggesting paleosoils and indicate unstable water balance.

Around 2450 cm (Unit VIII; ~170 ka) and 750–780 cm (Unit III; ~55–63 ka), Si/Al and K/Al peaks coincide with marked shifts in magnetic susceptibility (κ_{LF}) and minor increases in Ca values. In contrast to the peak at 128 ka, the overall rise in Si/Al ratios in upper Unit III and in the reddish-ocher, oxidized Unit II (from about 50 to

13 ka), which run parallel to an increase in detrital carbonate including gravels, undoubtedly occurred during a period of increasing local water deficit. Indeed, both lithofacies (Fig. 3) and decreasing AP/NAP pollen ratio which reaches its minimum values in Unit II between ~35 and 13 ka (corresponding to MIS2), suggest steppe-like vegetation on the watershed (Figs. 11b and 12b) and indicate that end of the last glacial period and Termination 1 coincide with one of the driest episode observed in the whole record. During this period, the Si/Al and the carbonate increases are attributed to intensification of wind-storm frequency or strength and of physical erosion rate in the watershed almost devoid of vegetation.

The local water deficit, documented during MIS2, may be due to a decrease in precipitation but the influence of local factors, such as topography and altitude, should also be considered. At present, freezing occurs three months a year at Yammoûneh. The number of freezing months was likely higher during glacial periods, when the altitudinal temperature lapse rate was enhanced in the Mediterranean regions (Kuhlemann et al., 2008). In the karstic Lake Ohrid (Albania), where the pollen record indicates wet/dry interglacials/glacial periods, respectively (Lézine et al., 2010), Belmecheri et al. (2009) have proposed that the formation of permafrost during glacials has

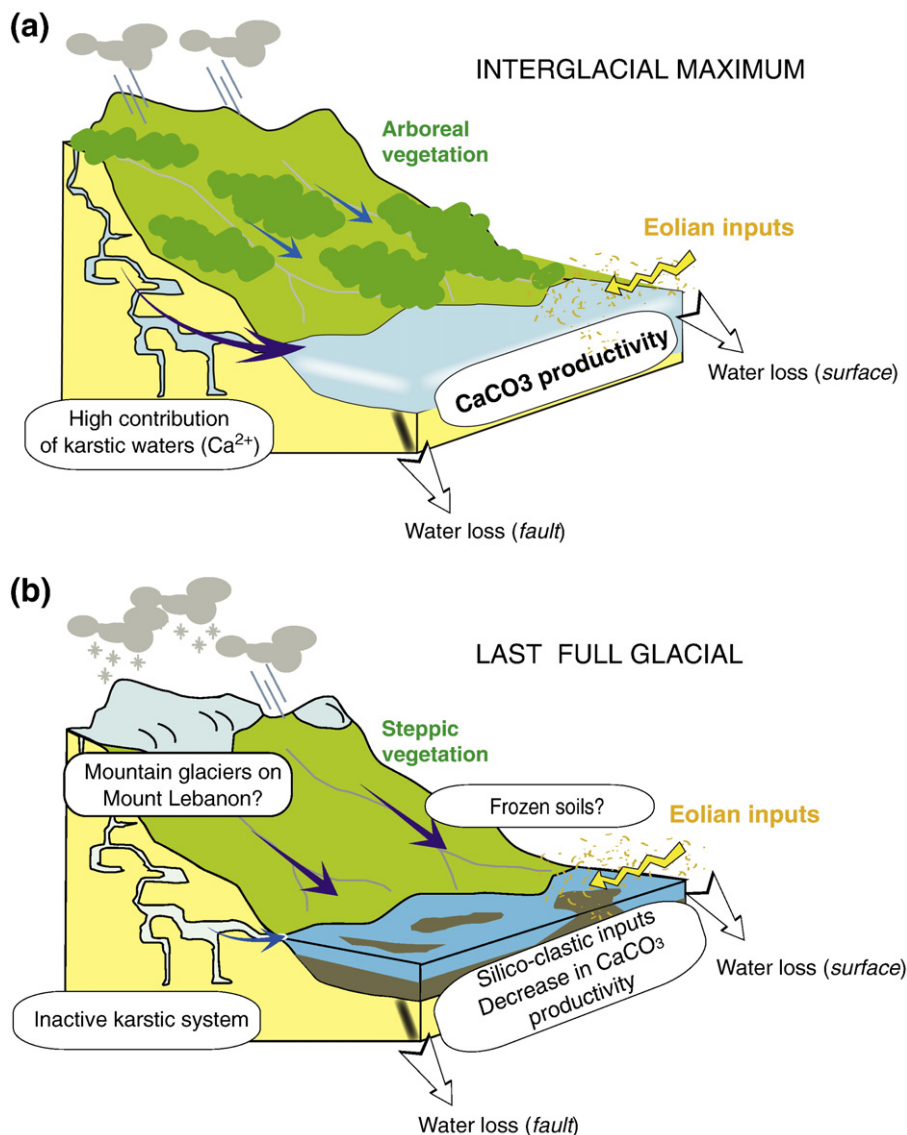


Fig. 12. Proposed scenarios for paleoenvironmental conditions during maximum interglacial and glacial periods.

prevented water infiltration into the karstic network, inducing the interruption of carbonate production. Such a process may have acted at Yammouneh during cold periods with a temperature departure (relative to modern) of -6 to -10 °C (Develle et al., 2010). The past existence of glaciers in Lebanon has for long remained questionable (Dubertret, 1975; Daëron, 2005). It seems now demonstrated by the study of moraine deposits (currently under ³⁶Cl dating) on the western slopes of Mount Lebanon (L. Benedetti, pers. comm.). Storage of snow-precipitation in the Mount Lebanon range as ice in permanent glaciers and frozen soils may have significantly decreased the liquid water inflows to the Yammouneh basin (Fig. 12b), water storage by ice does not mean necessarily that precipitation was considerably reduced. As for the interglacial periods, our interpretation of the glacial phases requires further analyses.

5.3. Comparison with some records from the Near East

Large uncertainties on core YAM04C' age model, especially prior to MIS 5, preclude detailed correlations with other records. Nevertheless, some comparisons can be made for dominant environmental conditions during the last interglacial optimum and full glacial conditions.

Assuming that our interpretations are correct, the Yammouneh sedimentary record indicates high water availability in the Yammouneh basin during interglacial optimum when the northern ice sheets and sea ice extent were reduced during periods of maximum insolation in the Northern Hemisphere and of maximum seasonal contrasts (Fig. 11). Phases of silt-clay accumulation suggest drier conditions, especially during MIS 2 and late MIS 3, although water availability was sufficient during MIS 6 and early MIS 4 to drain detrital particles from the watershed toward the basin floor.

For the early Holocene period, our interpretation is supported by other records from Lebanon. An early-mid Holocene wetting was evidenced in Lebanese low altitude areas from pollen data from the Bakka Plain (Hajar et al., 2008) and the 12 ka-speleothem $\delta^{18}\text{O}$ and $\delta^{13}\text{C}$ records from Jeita Cave, close to Beirut (Nader et al., 2007; Verheyden et al., 2008) (Fig. 1b). Such a wetting was also inferred from the pollen record from the Ghab Valley (Yasuda et al., 2000). This contrasts with the Dead Sea which remained very low (compared to glacial periods) during the Holocene (e.g., Enzel et al., 2003; Migowski et al., 2006).

On longer time scales, our findings appear in line with the 200 ka pollen record from Lake Urmia (Iran; Djamali et al., 2008) which shows wet-warm conditions during MIS 5 and MIS 1. Our record would be roughly in agreement with the Soreq and Peqiin cave

oxygen isotope records when interpreted in terms of precipitation amount (Bar-Matthews et al., 2003), but this view was firmly criticized by, e.g., Frumkin et al., 1999; Kolodny et al., 2005; Enzel et al., 2008). These authors consider that the speleothem $\delta^{18}\text{O}$ signal is primarily controlled by changes in the EM sea water isotopic composition. However, some others (Almogi-Labin et al., 2009) suggest that increased «rainfall amount» during interglacials represent the second order factor acting on these records. At Yammoûneh, Develle et al. (2010) have shown that, over the past 21 ka, the ^{18}O -depleted values of ostracod valves during the early Holocene reflect both the low $\delta^{18}\text{O}$ values of EM sea water and enhanced terrestrial rainfall, and that large glacial temperature departure has also been a major controlling factor. The long-term Yammoûneh $\delta^{18}\text{O}$ record will be discussed in a further paper.

Relatively dry local conditions during glacial periods, especially during late MIS 3 and early MIS 2, apparently conflict with lake stands in the Dead Sea Basin (Fig. 11e) reflecting higher precipitation. In our case, it is difficult to say if the local water deficit reflects water storage by ice or decreased precipitation. The first hypothesis implies a predominant influence of local factors (altitude and orographic barrier effects) in the Yammoûneh basin and water storage by ice (from 60 to 25 ka) to explain the differences between the two sites. The second hypothesis would imply changes in the NS rainfall gradients in the Levant at the glacial–interglacial timescale. Modifications in atmospheric circulation could explain such changes. Simulations by general circulation models (e.g., Lainé et al., 2009; Li and Battisti, 2008) show that the northern mid-latitude westerly belt was pushed southward during the LGM in response to ice sheet and sea ice extents at northern high latitudes, generating dry conditions in the northern Mediterranean basin. Enzel et al. (2008) have suggested that, under glacial conditions, the Mediterranean cyclones formed in winter over the northwest Mediterranean basin were forced to be funnelled along the Mediterranean directly east into the Levant, explaining the high Late Pleistocene lake-levels in the Dead Sea basin in glacial times.

6. Conclusions

Our study provides the first long paleoenvironmental record (~250 ka) in the northern Levant. The main points arising from the Yammoûneh record are as follows.

Sedimentary processes in the Yammoûneh basin was controlled by three major processes: (1) *in situ* lacustrine carbonate production, (2) erosion of the small surface watershed, (3) eolian inputs of allochthonous particles from remote sources.

During the warmest stages of interglacials periods, carbonate production in the lake reached its maximum, while siliciclastic material occurred in low amounts and was mainly of eolian origin. High lacustrine carbonate production, favoured by temperature and strong biological activity into the lake, is attributed to active water circulation through the Mnaïtra karstic system and enhanced spring water discharge. It is associated with the development of an arboreal vegetation cover limiting detrital inputs from the local watershed. This suggests relatively high precipitation amount in both the aquifer recharge zone and the surface catchment.

Siliciclastic particles from both eolian and local origins predominate during glacial intervals although moderate increases in carbonate and organic matter contents occurred by times. Physical erosion of the surface watershed was favoured by an open terrestrial vegetation cover. Reduced relative contribution of karstic spring water discharge limited *in situ* carbonate production. At least during the end of the last glacial period, these features indicate diminished liquid water availability in the Yammoûneh basin, due either to reduced precipitation or to water storage by ice under conditions much colder than today.

Our interpretation of the ca. 250 ka Yammoûneh record appears in agreement with climate fluctuations already evidenced in the northern Levant and in northern Near-East countries (e.g., Iran). Conversely, it apparently conflicts with lake-level fluctuations in the southern Levant, reflecting either a change in the NS precipitation gradient over the Levant, or a major role of local factors in the small Yammoûneh basin. Further analyses are, however, required to confirm our interpretations. A more comprehensive picture of the environmental evolution of the Yammoûneh area should be gained from the integration of other proxies analyzed independently on the same material, including detailed pollen record and the isotopic profile ($\delta^{18}\text{O}$ of ostracod valves) along the whole sequence.

Further work is also crucial to confirm and improve our age model, using other dating techniques (e.g., optically stimulated luminescence on quartz- or feldspars-rich levels). More chronological constraints may help to understand the high frequency variability observed in the banded clayey-silty intervals.

Supplementary materials related to this article can be found online at doi:10.1016/j.palaeo.2011.02.008.

Acknowledgement

We warmly acknowledge P. Tapponier, IPG-P, and A. Sursok, CNRG, Lebanon, who have initiated the Yammoûneh project and helped us in its realization. We thank M. Decobert and his team from the SETEL service (CEREGE) who have performed the coring. Thanks are due to C. Pailles from the CEREGE for her contribution to the coring trip, the opening and description of the core. We are grateful to J. Giraudeau and P. Martinez from the UMR EPOC, Bordeaux I University, for their help in the acquisition of XRF proxies. We thank A. Elias, American University in Beyrouth who kindly shared his large experience on the regional geology during our field expeditions, M. Desmet, Tours University, and M. Bar-Matthews, for fruitful discussions during the manuscript preparation. Support for this study came from the CNRS-France, the CNRS-Lebanon, the IPG-P, the French Embassy in Lebanon and the CEDRE French-Lebanese Program (convention no. 03 En F34/L42). We are grateful to reviewers who spent time to provide constructive comments and suggestions which helped us to deeply improve the manuscript.

References

- Abdel-Rahman, A.-F.M., 2002. Mesozoic volcanism in the Middle East: geochemical, isotopic and petrogenetic evolution of extension-related alkali basalts from central Lebanon. *Geol. Mag.* 139, 621–640.
- Abdel-Rahman, A.-F.M., Nassar, P.E., 2004. Cenozoic volcanism in the Middle East: petrogenesis of alkali basalts from northern Lebanon. *Geol. Mag.* 141, 545–563.
- Abi-Saleh, B., Safi, S., 1988. Carte de la végétation du Liban au 1/500000 + notice explicative. *Ecologia Mediterr.* XIV (1/2), 123–142.
- Almogi-Labin, A., Bar-Matthews, M., Shriki, D., Kolosovsky, E., Paterne, M., Schilman, B., Ayalon, A., Aizenshtat, Z., Matthews, A., 2009. Climatic variability during the last ~90 ka of the southern and northern Levantine Basin as evident from marine records and speleothems. *Quaternary Science Reviews* 28 (25–26), 2882–2896.
- Alpert, P., Ziv, B., 1989. The sharav cyclone: observations and some theoretical considerations. *J. Geophys. Res.* 94 (D15), 18,495–18,514.
- Aouad, A., Travi, Y., Blavoux, B., Job, J.O., Najem, D., 2004. Etude isotopique de la pluie et de la neige sur le Mont Liban: premiers résultats. *Hydrol. Sci.* 49, 429–441.
- Bar-Matthews, M., Ayalon, A., Kaufman, A., 1997. Late quaternary paleoclimate in the Eastern Mediterranean region from stable isotope analysis of speleothems at Soreq cave, Israel. *Quatern. Res.* 47, 155–168.
- Bar-Matthews, M., Ayalon, A., Gilmour, M., Matthews, A., Hawkesworth, C.J., 2003. Sea-level oxygen isotopic relationship from planktonic foraminifera and speleothems in the Eastern Mediterranean region and their implication for paleorainfall during interglacial intervals. *Geochim. Cosmochim. Acta* 67, 3181–3199.
- Bartov, Y., Goldstein, S.L., Mordechai, S., Enzel, Y., 2003. Catastrophic arid episodes in the Eastern Mediterranean linked with the North Atlantic Heinrich events. *Geological Society of America* 31 (5), 439–442.
- Bar-Yosef, O., 2003. *The Origins of Modern Humans*. Continuum, London.
- Bathurst, R.G.C., 1975. Carbonate sediments and their diagenesis (second enlarged edition). *Developments in Sedimentology*. Elsevier, New York.
- Belmecheri, S., Namiotko, T., Robert, C., Grafenstein, U., Danielopol, D.L., 2009. Climate controlled ostracod preservation in Lake Ohrid (Albania, Macedonia). *Palaeogeography Palaeoclimatology Palaeoecology* 277 (3–4), 236–245.

- Besançon, J., 1968. Le poljé de Yammoûneh. *Rev. Liban. géographie Hannon* 3, 3–62.
- Channell, J.E.T., Hodell, D.A., Xuan, C., Mazaud, A., Stoner, J.S., 2009. Age calibrated relative paleointensity for the last 1.5 Myr at IODP Site U1308 (North Atlantic). *Earth Planet. Sci. Lett.* 274, 59–71.
- Croudace, I.W., Rindby, A., Rothwell, R.G., 2006. ITRAX: description and evaluation of a new multi-function X-ray core scanner. *Geol. Soc. Lond. Spec. Publ.* 267, 51–63.
- Crouvi, O., Amit, R., Enzel, Y., Porat, N., Sandler, A., 2008. Sand dunes as a major proximal dust source for late Pleistocene loess in the Negev Desert, Israel. *Quatern. Res.* 70, 275–282.
- Daéron, M., 2005. Rôle, cinématique et comportement sismique à long terme de la faille de Yammoûneh, principale branche décrochante du coude transpressif libanais (faille du Levant) UNUniversity of Paris VII.
- Daéron, M., Benedetti, L., Tapponnier, P., Sursock, A., Finkel, R.C., 2004. Constraints on the post-25-ka slip rate of the Yammouneh fault (Lebanon) using in situ cosmogenic Cl-36 dating of offset limestone-clast fans. *Earth Planet. Sci. Lett.* 227, 105–119.
- Daéron, M., Klingler, Y., Tapponnier, P., Elias, A., Jacques, E., Sursock, A., 2007. 12,000-year-long record of 10 to 13 paleoearthquakes on the Yammouneh fault, Levant fault system, Lebanon. *Bull. Seismol. Soc. Am.* 97, 749–771.
- Dayan, U., Ziv, B., Shooob, T., Enzel, Y., 2008. Suspended dust over southeastern Mediterranean and its relation to atmospheric circulations. *Int. J. Climatol.* 28, 915–924.
- Dean, W.E., 1974. Determination of carbonate and organic matter in calcareous sediments and sedimentary rocks by loss on ignition: Comparison with other methods. *J. Sed. Petrol.* 44, 242–248.
- Dean, W.E., 1999. The carbon cycle and biogeochemical dynamics in lake sediments. *J. Paleolimnol.* 21, 375–393.
- Demory, F., Nowaczyk, N.R., Witt, A., Oberhänsli, H., 2005. High-resolution magnetostratigraphy of late quaternary sediments from Lake Baikal, Siberia: timing of intracontinental paleoclimatic responses. Global and planetary change progress towards reconstructing past climate in Central Eurasia, with special emphasis on Lake Baikal, 46, pp. 167–186.
- Develle, A.-L., Herreros, J., Vidal, L., Sursok, A., Gasse, F., 2010. Controlling factors on a paleo-lake oxygen isotope record (Yammoûneh, Lebanon) since the Last Glacial Maximum. *Quatern. Sci. Rev.* 186, 416–425.
- Djamali, M., de Beaulieu, J.-L., Shah-hosseini, M., Andrieu-Ponel, V., Ponel, P., Amini, A., Akhiani, H., Leroy, S.A.G., Stevens, L., Lahijani, H., Brewer, S., 2008. A late Pleistocene long pollen record from Lake Urmia, NW Iran. *Quatern. Res.* 69 (3), 413–420.
- Dubertret, L., 1975. Introduction à la carte géologique au 1/50 000 du Liban. *Notes Mém. Moyen Orient* 13, 345–403.
- Effler, S.W., 1987. The importance of whiting as a component of raw water turbidity. *J. Am. Water Works Assn.* 79, 80–82.
- El-Hakim, M., 2005. Les aquifères karstiques de l'Anti-Liban et du nord de la plaine de la Bekaa: caractéristiques, fonctionnement, évolution et modélisation, d'après l'exemple du système karstique Anjarchamsine (Liban). Université de Montpellier II et Université Saint Joseph de Beyrouth, 216.
- Emeis, K.C., Schulz, H., Struck, U., Rossignol-Strick, M., Erlenkeuser, H., Howell, M.W., Kroon, D., Mackensen, A., Ishizuka, S., Oba, T., Sakamoto, T., Koizumi, I., 2003. Eastern Mediterranean surface water temperatures and delta O-18 composition during deposition of sapropels in the late Quaternary. *Paleoceanography* 18 (1).
- Enzel, Y., Bookman, R., Sharon, D., Gvirtzman, H., Dayan, U., Baruch, Z., Mordechai, S., 2003. Late Holocene climates of the Near East deduced from Dead Sea level variations and modern regional winter rainfall. *Quaternary Research* 60 (3), 263–373.
- Enzel, Y., Amit, R., Dayan, U., Crouvi, O., Kahana, R., Baruch, Z., Sharon, D., 2008. The climatic and physiographic controls of the eastern Mediterranean over the late Pleistocene climates in the southern Levant and its neighboring deserts. *Glob. Planet. Change* 60, 165–192.
- Essallami, L., Sicre, M.A., Kallel, N.L.L., Siani, G., 2007. Hydrological changes in the Mediterranean Sea over the last 30,000 years. *Geochemistry Geophysics Geosystems* 8 (7).
- Fang, X.-M., Li, J.-J., Van der Voo, R., Mac Niocaill, C., Dai, X.-R., Kemp, R.A., Derbyshire, E., Cao, J.-X., Wang, J.-M., Wang, G., 1997. A record of the Blake Event during the last interglacial paleosol in the western Loess Plateau of China. *Earth Planet. Sci. Lett.* 146, 73–82.
- Frumkin, A., Stein, M., 2004. The Sahara-East Mediterranean dust and climate connection revealed by strontium and uranium isotopes in a Jerusalem speleothem. *Earth Planet. Sci. Lett.* 217, 451–464.
- Frumkin, A., Ford, D.C., Schwarcz, H.P., 1999. Continental oxygen isotopic record of the last 170,000 years in Jerusalem. *Quatern. Res.* 51, 317–327.
- Gat, J.R., Klein, B., Kushnir, Y., Roether, W., Wernli, H., Yam, R., Shemesh, A., 2003. Isotope composition of air moisture over the Mediterranean Sea: an index of the air-sea interaction pattern. *Tellus B Chem. Phys. Meteorol.* 55, 953–965.
- Goudie, A.S., Middleton, N.J., 2001. Saharan dust storms: nature and consequences. *Earth Sci. Rev.* 56, 179–204.
- Guillou, H., Singer, B.S., Laj, C., Kissel, C., Scaillet, S., Jicha, B.R., 2004. On the age of the Laschamp geomagnetic excursion. *Earth Planet. Sci. Lett.* 227, 331–343.
- Hakim, B., 1985. Recherches hydrologiques et hydrochimiques sur quelques karsts méditerranéens du Liban, Syrie et Maroc. Beyrouth, Liban: Université Libanaise, Section des Etudes Géographiques, 701.
- Hajar, L., Khater, C., Cheddadi, R., et al., 2008. Vegetation changes during the late Pleistocene and Holocene in Lebanon: a pollen record from the Bekaa Valley. *Holocene* 18 (7), 1089–1099.
- Hamann, Y., Ehrmann, W., Schmiedl, G., Krüger, S., Stuut, J.B., Kuhnt, T., 2008. Sedimentation processes in the Eastern Mediterranean Sea during the Late Glacial and Holocene revealed by end-member modelling of the terrigenous fraction in marine sediments. *Marine Geology* 248 (1–2), 97–114.
- Henry, D.O., 2003. Behavioral organization and the beginning of human modernity. *Continuum* 2003, 312 pp.
- Herrero-Bervera, E., Hellsley, C.E., Sarna-Wojcicki, A.M., Lajoie, K.R., Meyer, C.E., McWilliams, M.O., Negrini, R.M., Turrin, B.D., Nolan, J.M.D., Liddicoat, J.C., 1994. Age and correlation of a paleomagnetic episode in the western United States by ⁴⁰Ar/³⁹Ar dating and tephrochronology: the Jamaica, Blake, or a new polarity episode? *J. Geophys. Res.* 99.
- Hrouda, F., 1982. Magnetic anisotropy of rocks and its application in geology and geophysics. *Surv. Geophys.* 5, 37–82.
- Ihaka, R., Gentleman, R., 1996. R: a language for data analysis and graphics. *J. Comput. Graph. Stat.* 5, 299–314.
- Imbrie, J., Hays, J.D., Martinson, D.G., Mcintyre, A., Mix, A.C., Morley, J.J., Pisias, N.G., W.L., P., Shackleton, N.J., 1984. The orbital theory of Pleistocene climate: support from revised chronology of the marine 180 record. Reidel, Dordrecht.
- Johnson, H.P., Kinoshita, H., Merrill, R.T., 1975. Rock magnetism and paleomagnetism of some north Pacific deep-sea sediments. *Geol. Soc. Am. Bull.* 86, 412–420.
- Kahana, R., Ziv, B., Enzel, Y., Dayan, U., 2002. Synoptic climatology of major floods in the Negev Desert, Israel. *Int. J. Climatol.* 22, 867–882.
- Karam, F., 2002. Climate change and variability in Lebanon: impact on land use and sustainable agriculture development. Proceedings of the first technical workshop of the "Mediterranean" component of CLIMAGRI project on climate change and agriculture, FAO, pp. 25–27. September. Rome.
- Kaufman, A., 1993. An evaluation of several methods for determining ages in impure carbonates. *Geochim. Cosmochim. Acta* 57, 2303–2317.
- Kelts, K., Hsü, K., 1978. Freshwater carbonate sedimentation. In: Lerman, A. (Ed.), *Lakes: Chemistry, Geology, Physics*. Springer, New York, pp. 295–323.
- Kelts, K., Talbot, M.R., 1990. Lacustrine carbonates as geochemical archives of environmental change and biotic-abiotic interactions. In: M. M. T. a. C. S. (Ed.), *Large Lakes: Ecological Structure and Function*. Springer-Verlag, pp. 288–315.
- Kolodny, Y., Mordechai, S., Machlus, M., 2005. Sea-rain-lake relation in the Last Glacial East Mediterranean revealed by $\delta^{18}\text{O}$ - $\delta^{13}\text{C}$ in Lake Lisan aragonites. *Geochimica et Cosmochimica Acta* 69, 4045–4060.
- Kuhlemann, J., Rohling, E.J., Krumrei, I., Kubik, P., Ivy-Ochs, S., Kucera, M., 2008. Regional synthesis of Mediterranean atmospheric circulation during the Last Glacial Maximum. *Science* 321, 1338–1340.
- Lainé, A., Kageyama, M., Salas-Melia, D., Voldoire, A., Riviere, G., Ramstein, G., Planton, S., Tyteca, S., Peterschmitt, J.Y., 2009. Northern hemisphere storm tracks during the last glacial maximum in the PMIP2 ocean-atmosphere coupled models: energetic study, seasonal cycle, precipitation. *Clim. Dyn.* 32 (5), 593–614.
- Lamouroux, M., 1972. Etudes des sols formés sur roches carbonatées. *Pedogenèse fersiallitique au Liban*. Paris, 259.
- Le Pichon, X., Gaulier, J.M., 1988. The rotation of Arabia and the Levant fault system. *Tectonophysics* 153, 271–294.
- Lézine, A.M., von Grafenstein, U., Andersen, N., Belmecheri, S., Bordon, A., Caron, B., Cazet, J.P., Erlenkeuser, H., Fouache, E., Grenier, C., Huntsman-Mapila, P., Hureau-Mazaudier, D., Manelli, D., Mazaud, A., Robert, C., Sulpizio, R., Tiercelin, J.J., Zanchetta, G., Zeqollari, Z., 2010. Lake Ohrid, Albania, provides an exceptional multi-proxy record of environmental changes during the last glacial-interglacial cycle. *Palaeogeogr. Palaeoclimatol. Palaeoecol.* 287, 116–127.
- Li, C., Battisti, D.S., 2008. Reduced Atlantic storminess during last glacial maximum: Evidence from a coupled climate model. *J. Clim.* 21 (14), 3561–3579.
- Liban, S.m.d., 1973. Atlas climatique du Liban. Observatoire de Ksara, Beyrouth.
- Lund, S. P. & S. K. Banerjee (1979) Paleosecular variations from lake sediments. *Journal Name: Rev. Geophys. Space Phys.; (United States); Journal Volume: 17:2, Medium: X; Size: Pages: 244–249*
- Martin-Hernandez, F., Luneburg, C.M., Aubourg, C., Jackson, M., 2004. Magnetic fabric: methods and applications — an introduction. *Geol. Soc. Lond. Spec. Publ.* 238, 1–7.
- Martinson, D.G., Pisias, N.G., Hays, J.D., Imbrie, J., Moore, T.C., Shackleton, N.J., 1987. Age dating and the orbital theory of the ice ages: Development of a high-resolution 0 to 300,000-year chronostratigraphy. *Quatern. Res.* 27, 1–29.
- Migowski, C., Stein, M., Prasad, S., Negendank, J.F.W., Agnon, A., 2006. Holocene climate variability and cultural evolution in the Near East from the Dead Sea sedimentary record. *Quaternary Research Holocene Climate and Cultural Evolution in Late Prehistoric-Early Historic West Asia*, 66, pp. 421–431.
- Mullins, H.T., 1998. Environmental change controls of lacustrine carbonate, Cayuga Lake, New York. *Geology* 26, 443–446.
- Nader, F.H., Verheyden, S., Cheng, H., Swennen, R., 2007. Etude pétrographique et géochimique d'une stalagmite de la grotte de Jeita (Liban). *Lebanese Science Journal* 8 (2), 45–58.
- Oda, H., Nakamura, K., Ikehara, K., Nakano, T., Nishimura, M., Khlystov, O., 2002. Paleomagnetic record from Academician Ridge, Lake Baikal: a reversal excursion at the base of marine oxygen isotope stage 6. *Earth Planet. Sci. Lett.* 202, 117–132.
- Rochette, P., Vadeboin, F., Clochard, L., 2001. Rock magnetic applications of Halbach cylinders. *Phys. The Earth Planet. Inter.* 126, 109–117.
- Romero, L., Camacho, A., Vicente, E., Miracle, M., 2006. Sedimentation patterns of photosynthetic bacteria based on pigment markers in meromictic lake La Cruz (Spain): paleolimnological implications. *J. Paleolimnol.* 35, 167–177.
- Saaroni, H., Ziv, B., Bitan, A., Alpert, P., 1998. Easterly wind storms over Israel. *Theor. Appl. Climatol.* 59, 61–77.
- Shane, P., Black, T., Westgate, J., 1994. Isothermal plateau fission-track age for a paleomagnetic excursion in the Mamaku Ignimbrite, New Zealand, and implications for Late Quaternary stratigraphy. *Geophys. Res. Lett.* 21, 1695–1698.
- Sharon, D., Kutiel, H., 1986. The distribution of rainfall intensity in Israel, its regional and seasonal variations and its climatological evaluation. *J. Climatol.* 6, 277–291.

- Stacey, F.D., Joplin, G., Lindsay, J., 1960. Magnetic anisotropy and fabrics of some foliated rocks from S. E. Australia. *Geofiz. Pura Appl.* 47, 30–40.
- Stanley, D.J., Wingerath, J.G., 1996. Clay mineral distributions to interpret Nile cell provenance and dispersal. 1. Lower river Nile to delta sector. *J. Coast. Res.* 12, 911–929.
- Staubwasser, M., Weiss, H., 2006. Holocene climate and cultural evolution in late prehistoric–early historic West Asia. *Quatern. Res.* 66, 372–387.
- Tauxe, L., 1993. Sedimentary records of relative paleointensity of the geomagnetic field—theory and practice. *Rev. Geophys.* 31, 319–354.
- Thompson, R., Oldfield, F., 1986. *Environmental Magnetism*. Allen and Unwin, London.
- Thompson, R., Bloemendal, J., Dearing, J.A., Oldfield, F., Rummery, T.A., Stober, J.C., Turner, G.M., 1980. Environmental applications of magnetic measurements. *Science* 207, 481–486.
- Thouveny, N., Carcaillet, J., Moreno, E., Leduc, G., Nérini, D., 2004. Geomagnetic moment variation and paleomagnetic excursions since 400 kyr BP: a stacked record from sedimentary sequences of the Portuguese margin. *Earth and Planetary Science Letters* 219, 377–396.
- Tsoar, H., Pye, K., 1987. Dust transport and the question of desert loess formation. *Sedimentology* 34, 139–153.
- Tzedakis, P.C., 1993. Long-term tree populations in northwest Greece through multiple Quaternary climatic cycles. *Nature* 364 (6436), 437–440.
- Vaks, A., 2007b. Quaternary paleoclimate of north-eastern boundary of the Saharan Desert: reconstruction from speleothems of Negev Desert, Israel. PhD thesis. The Hebrew University, 211 pp.
- Vaks, A., Bar-Matthews, M., Ayalon, A., Schilman, B., Gilmour, M., Hawkesworth, C.J., Frumkin, A., Kaufman, A., Matthews, A., 2003. Paleoclimate reconstruction based on the timing of speleothem growth and oxygen and carbon isotope composition in a cave located in the rain shadow in Israel. *Quatern. Res.* 59, 182–193.
- Vaks, A., Bar-Matthews, M., Ayalon, A., Matthews, A., Frumkin, A., Dayan, U., Halicz, L., Almogi-Labin, A., Schilman, B., 2006. Paleoclimate and location of the border between Mediterranean climate region and the Saharo-Arabian desert as revealed by speleothems from northern Negev desert, Israel. *Earth Planet. Sci. Lett.* 249, 384–399.
- Vaks, A., Bar-Matthews, M., Ayalon, A., Matthews, A., Halicz, L., Frumkin, A., 2007. Desert speleothems reveal climatic window for African exodus of early modern humans. *Geology* 35, 831–834.
- Vaks, A., Bar-Matthews, M., Ayalon, A., Matthews, A., Frumkin, A., 2008. Relations between Mediterranean cyclones and African Monsoon from speleothems of Negev Desert, Israel. *Geochim. Cosmochim. Acta* 72, A969–A.
- Verheyden, S., Nader, F.H., Cheng, H.J., Edwards, L.R., Swennen, R., 2008. Paleoclimate reconstruction in the Levant region from the geochemistry of a Holocene stalagmite from the Jeita cave, Lebanon. *Quatern. Res.* 70 (3), 368–381.
- Waldmann, N., Torfstein, A., Stein, M., 2010. Northward intrusions of low and mid latitude storms across the Saharo-Arabian belt during past interglacials. *Geology* 38, 567–570.
- Winstanley, D., 1972. *Sharav*. *Weather* 27, 146–148.
- Wu, H.B., Guiot, J.L., Brewer, S., Guo, Z.T., 2007. Climatic changes in Eurasia and Africa at the last glacial maximum and mid-Holocene: reconstruction from pollen data using inverse vegetation modelling. *Clim. Dyn* 29 (2–3), 211–229.
- Yasuda, Y., Kitagawa, H., Nakagawa, T., 2000. The earliest record of major anthropogenic deforestation in the Ghab Valley, Syria: a palynological study. The earliest record of major anthropogenic deforestation in the Ghab Valley, Syria: a palynological study. *Quaternary International* 73/74, 127–136.
- Zabel, M., Schneider, R.R., Wagner, T., Adegbe, A.T., de Vries, U., Kolonic, S., 2001. Late Quaternary climate changes in Central Africa as inferred from terrigenous input to the Niger Fan. *Quatern. Res.* 56, 207–217.
- Ziv, B., Dayan, U., Sharon, D., 2005. A mid-winter, tropical extreme flood-producing storm in southern Israel: synoptic scale analysis. *Meteorol. Atmos. Phys.* 88, 53–63.
- Ziv, B., Dayan, U., Kuschnir, Y., Roth, C., Enzel, Y., 2006. Regional and global atmospheric patterns governing rainfall in the southern Levant. *Int. J. Climatol.* 26, 55–73.
- Ziv, B., Saaroni, H., Romem, M., Heifetz, E., Harnik, N., Baharad, A., 2010. Analysis of conveyor belts in winter Mediterranean cyclones. *Theor. Appl. Climatol.* 99, 441–455.